Article

Neuron

m^6A mRNA Methylation Is Essential for Oligodendrocyte Maturation and CNS Myelination

Highlights

- Oligodendrocyte maturation is accompanied by modifications in m^6A mRNA methylation
- m^6A mRNA methylation is required for oligodendrocyte maturation and CNS myelination
- m^6A mRNA methylation regulates the transcriptomes of oligodendrocyte lineage cells
- Proper *neurofascin* mRNA splicing in oligodendrocytes requires m^6A methylation

Authors

Huan Xu, Yulia Dzhashiashvili, Ankeeta Shah, ..., Guo-li Ming, Chuan He, Brian Popko

Correspondence

brian.popko@northwestern.edu

In Brief

Xu et al. show that oligodendrocyte development is associated with dynamic changes in posttranscriptional mRNA methylation. Moreover, they demonstrate that the m^6A epigenetic RNA mark has considerable impact on the myelinating cell's transcriptome and is essential for normal CNS myelination.

Xu et al., 2020, Neuron *105*, 293–309
January 22, 2020
https://doi.org/10.1016/j.neuron.2019.12.013

CellPress

Neuron
Article

m^{6}A mRNA Methylation Is Essential for Oligodendrocyte Maturation and CNS Myelination

Huan Xu,[1,7] Yulia Dzhashiashvili,[1] Ankeeta Shah,[2,3] Rejani B. Kunjamma,[1,7] Yi-lan Weng,[4] Benayahu Elbaz,[1,7] Qili Fei,[5] Joshua S. Jones,[1] Yang I. Li,[3] Xiaoxi Zhuang,[6] Guo-li Ming,[4] Chuan He,[5] and Brian Popko[1,7,8,*]
[1]Center for Peripheral Neuropathy and Department of Neurology, University of Chicago, Chicago, IL 60637, USA
[2]Committee on Genetics, Genomics, and Systems Biology, University of Chicago, Chicago, IL 60637, USA
[3]Section of Genetic Medicine, Department of Medicine, University of Chicago, Chicago, IL 60637, USA
[4]Department of Neuroscience and Mahoney Institute for Neurosciences, Institute for Regenerative Medicine, Perelman School of Medicine, University of Pennsylvania, Philadelphia, PA 19104, USA
[5]Department of Chemistry and Institute for Biophysical Dynamics, University of Chicago, Chicago, IL 60637, USA
[6]Department of Neurobiology, University of Chicago, Chicago, IL 60637, USA
[7]Present address: Department of Neurology, Northwestern University Feinberg School of Medicine, Chicago, IL 60611, USA
[8]Lead Contact
*Correspondence: brian.popko@northwestern.edu
https://doi.org/10.1016/j.neuron.2019.12.013

SUMMARY

The molecular mechanisms that govern the maturation of oligodendrocyte lineage cells remain unclear. Emerging studies have shown that N^6-methyladenosine (m^{6}A), the most common internal RNA modification of mammalian mRNA, plays a critical role in various developmental processes. Here, we demonstrate that oligodendrocyte lineage progression is accompanied by dynamic changes in m^{6}A modification on numerous transcripts. *In vivo* conditional inactivation of an essential m^{6}A writer component, METTL14, results in decreased oligodendrocyte numbers and CNS hypomyelination, although oligodendrocyte precursor cell (OPC) numbers are normal. *In vitro Mettl14* ablation disrupts postmitotic oligodendrocyte maturation and has distinct effects on OPC and oligodendrocyte transcriptomes. Moreover, the loss of *Mettl14* in oligodendrocyte lineage cells causes aberrant splicing of myriad RNA transcripts, including those that encode the essential paranodal component neurofascin 155 (NF155). Together, our findings indicate that dynamic RNA methylation plays an important regulatory role in oligodendrocyte development and CNS myelination.

INTRODUCTION

Oligodendrocytes are glial cells in the CNS that are responsible for myelination of axons, which allows for rapid saltatory conduction (Nave and Werner, 2014; Simons and Nave, 2015). Oligodendrocytes develop from oligodendrocyte precursor cells (OPCs), which originate from discrete regions of the embryonic neural tube (Rowitch, 2004). To become mature myelinating oligodendrocytes, OPCs first exit the proliferation state and differentiate into premyelinating oligodendrocytes, resulting in the expression of major myelinating proteins such as myelin basic protein (MBP) and proteolipid protein (PLP). A series of morphological changes then allows these oligodendrocytes to extend a number of processes that wrap axons with the multilayered myelin sheath (Zuchero and Barres, 2015). Elucidating the key events involved in oligodendrocyte lineage progression is critical to understand the cellular and developmental biology of myelin production and regeneration.

Following a defined series of steps, oligodendrocyte lineage progression is tightly controlled in time and space (Liu et al., 2016). However, the exact mechanism by which oligodendrocyte lineage progression is regulated has yet to be fully elucidated. A number of intrinsic and extrinsic factors have been found to be critical for regulating oligodendrocyte development. Growth factors, such as Sonic hedgehog (Shh), bone morphogenetic proteins (BMPs), and platelet-derived growth factor (PDGF), have been shown to influence the maturation of oligodendrocyte lineage cells from early progenitors to mature, myelinating cells (Nishiyama et al., 2009). Transcription factors, such as Nkx-2.2, Olig1, Olig2, Sox10, Myrf, and ZFP24, are required for maturation of oligodendrocytes (Elbaz and Popko, 2019; Mitew et al., 2014). In addition, epigenetic mechanisms including chromatin remodeling by DNA methylation, histone deacetylases, and gene silencing by non-coding RNAs have been shown to play critical roles in oligodendrocyte differentiation and function during development and remyelination (Li and Richardson, 2009; Marin-Husstege et al., 2002; Moyon and Casaccia, 2017; Ye et al., 2009; Zhao et al., 2010b).

Although reversible chemical modification of DNA and histone proteins is known to influence gene expression and a multitude of biological processes, a similar role for the chemical modification of RNA has only recently been identified (Fu et al., 2014). The discovery of reversible *N*^{6}-methyladenosine (m^{6}A) mRNA methylation has revealed a new dimension of post-transcriptional regulation of gene expression (Yue et al., 2015). Emerging studies have demonstrated that this m^{6}A "mark" influences

various aspects of mRNA metabolism, including stability, translation, localization, and splicing (Roundtree et al., 2017; Wang et al., 2014; Xiao et al., 2016; Zhao et al., 2014; Zhou et al., 2018). By controlling the turnover and/or translation of transcripts during cell-state transitions, m^{6}A modification of mRNA plays key regulatory roles during embryonic and adult stem cell differentiation (Frye et al., 2018). Recent studies have highlighted the function of m^{6}A in lineage fate decisions during cell development, such as embryonic stem cell pluripotency exit, T cell differentiation, hematopoietic fate transition, and gametogenesis (Batista et al., 2014; Geula et al., 2015; Ivanova et al., 2017; Li et al., 2017; Weng et al., 2018b; Xu et al., 2017; Zhang et al., 2017). Importantly, a recent study in neural stem cells revealed that conditional inactivation of the gene that encodes METTL14, a core component of the m^{6}A methyltransferase complex (Liu et al., 2014), disrupts cortical neurogenesis (Yoon et al., 2017), thus revealing a critical role of the m^{6}A mark in CNS neuronal development.

In this study, we sought to elucidate the role that m^{6}A mRNA methylation plays in oligodendrocyte lineage progression by conditionally inactivating the *Mettl14* gene specifically in these cells using a *Mettl14* conditional (floxed) mouse line in combination with oligodendrocyte Cre driver lines. *In vivo*, we found myelin abnormalities and altered oligodendrocyte numbers in the *Mettl14* mutants. Despite these findings, OPC numbers were not affected. *In vitro*, OPCs lacking *Mettl14* did not properly differentiate into mature oligodendrocytes, suggesting that m^{6}A plays a critical role in oligodendrocyte differentiation. RNA sequencing (RNA-seq) and m^{6}A-seq revealed that OPC and oligodendrocyte transcripts encoding transcription factors, DNA epigenetic regulators, and signaling pathways that are critical for oligodendrocyte lineage progression were m^{6}A marked and differentially affected by the *Mettl14* deletion. We also found pervasive, aberrant mRNA splicing in the *Mettl14*-deleted OPCs and oligodendrocytes. Importantly, we discovered that the critical paranode component NF155 is differentially spliced and significantly disrupted during myelination in the *Mettl14*-ablated mutants.

RESULTS

Oligodendrocyte Lineage Progression Is Accompanied by Changes in m^{6}A Modification on Numerous Transcripts

To characterize changes of the m^{6}A mark and its role in gene expression during oligodendrocyte lineage progression, we performed m^{6}A-seq and RNA-seq on both purified OPCs and mature, cultured oligodendrocytes. Using an immunopanning approach (Emery and Dugas, 2013), we purified OPCs from neonatal mouse pups. These cells were maintained under proliferating conditions with the addition of the OPC mitogen PDGF-AA. We obtained mature oligodendrocytes by promoting OPC differentiation via removal of PDGF-AA and addition of the T3 hormone to the culture media (Figure 1A). SMART2 single-cell RNA-seq was used for m^{6}A mRNA profiling (Picelli et al., 2014; Weng et al., 2018b), which detected 3,554 m^{6}A-marked transcripts in OPCs and 2,606 m^{6}A-marked transcripts in oligodendrocytes. Gene ontology analyses indicated that these m^{6}A-marked transcripts have important functions for cell development in both OPCs (Figure 1B) and oligodendrocytes (Figure 1C). The m^{6}A-seq data also revealed transcripts present in both OPCs and oligodendrocytes that were differentially marked by m^{6}A, demonstrating the dynamic nature of this mRNA modification. We found 2,806 transcripts with the m^{6}A mark in OPCs that were present but not marked in oligodendrocytes (Figure 1D) and 1,626 transcripts that possessed the m^{6}A mark in oligodendrocytes but not in OPCs (Figure 1E). Only 23 of the shared transcripts (Figure 1F) showed the m^{6}A mark in both OPCs and oligodendrocytes. The dynamic nature of the m^{6}A mark in oligodendrocyte lineage cells suggests that it may play an important role in regulating oligodendrocyte differentiation and CNS myelination.

In order to investigate the role of the m^{6}A mark in CNS myelinating cells, we generated mouse lines in which the gene encoding an essential m^{6}A writer component, METTL14, was conditionally inactivated at distinct oligodendrocyte developmental stages. We crossed mice carrying a conditional allele of *Mettl14* (*Mettl14*$^{fl/fl}$) (Koranda et al., 2018) with mice expressing the Cre recombinase under the transcriptional control of oligodendrocyte transcription factor 2 (Olig2), which is expressed throughout the oligodendrocyte lineage (Schüller et al., 2008) (Figure 1G). The *Mettl14*$^{fl/fl}$*;Olig2*-Cre mouse line allows us to study the role of m^{6}A in developing oligodendrocyte lineage cells (Bergles and Richardson, 2015). We also generated *Mettl14*$^{fl/fl}$*;CNP*-Cre mice (Figure 1G), in which *Mettl14* is conditionally eliminated by Cre under the transcriptional control of the myelin protein CNP primarily in postmitotic oligodendrocytes (Lappe-Siefke et al., 2003), allowing us to study the role of m^{6}A in maturing oligodendrocytes.

Mettl14 Ablation Leads to Reduction of Mature Oligodendrocytes, but Not OPCs

We first examined whether the *Mettl14* gene was efficiently inactivated via the Cre-*loxP* genetic strategy by examining METTL14 expression in the CNS using immunohistochemistry. We observed a reduction of METTL14 expression in both *Mettl14*$^{fl/fl}$*;Olig2*-Cre and *Mettl14*$^{fl/fl}$*;CNP*-Cre mutants, compared to their *Mettl14*$^{fl/fl}$ littermate controls at postnatal day 12 (P12) (Figures S5A–S5F), and across different CNS white matter regions at P18 (data not shown), a time point at which myelin is still undergoing development.

To gain insight into how *Mettl14* inactivation affects oligodendrocyte lineage cell development, we used immunohistochemistry to detect the oligodendrocyte lineage cell marker Olig2 in P18 mice (Figures 2A and 2B). We found a decreased percentage of Olig2/METTL14 double-positive cells (Figure 2C) accompanied by a reduction of Olig2+ cell numbers in the corpus callosum in *Mettl14*$^{fl/fl}$*;Olig2*-Cre (Figure 2D) mutants. Similarly, P18 *Mettl14*$^{fl/fl}$*;CNP*-Cre (Figures S1A and S1B) mutants also showed decreased percentage of Olig2/METTL14 double positive cells (Figure S1C) and decreased Olig2+ cell numbers (Figure S1D) and in the corpus callosum. The reduction of oligodendrocyte lineage cells in both *Mettl14*$^{fl/fl}$*;Olig2*-Cre and *Mettl14*$^{fl/fl}$*;CNP*-Cre mutant corpus callosum indicates that *Mettl14* is important in oligodendrocyte lineage development.

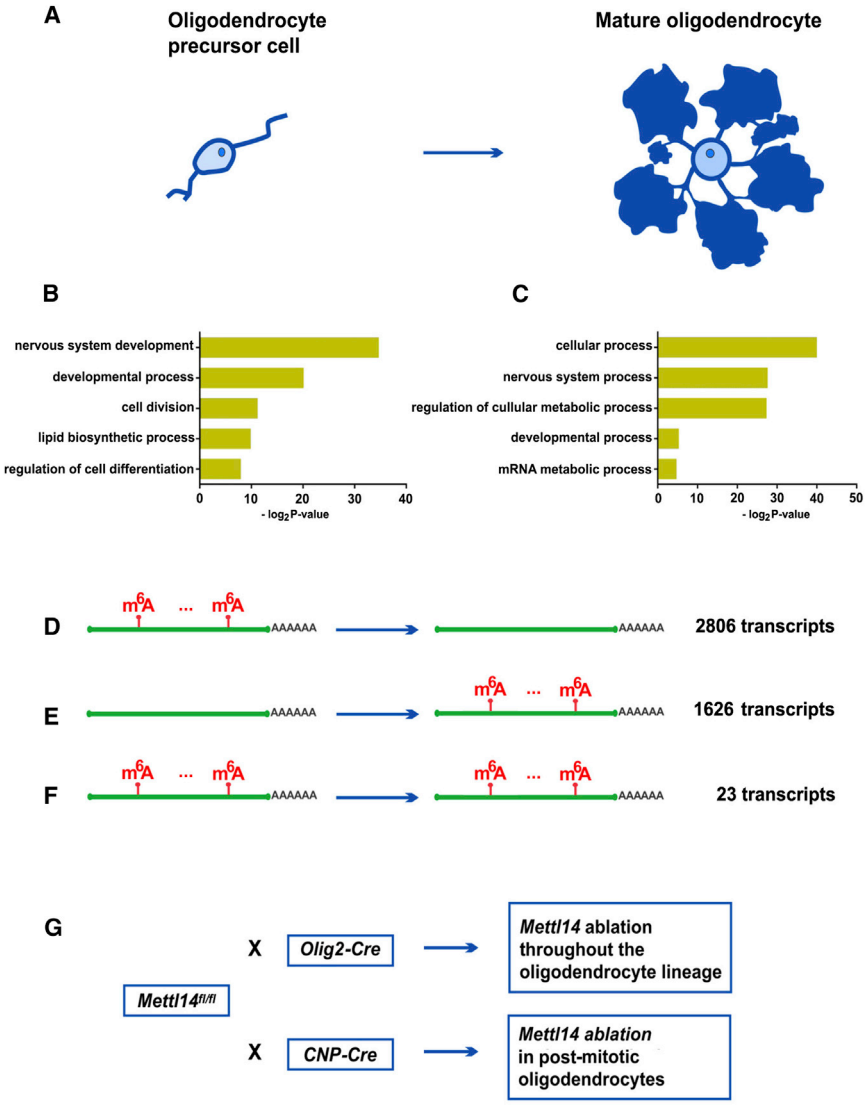

Figure 1. Oligodendrocyte Lineage Progression Is Accompanied by Changes in m^{6}A Modification on Numerous Transcripts

(A) Schematic drawing of an OPC and mature oligodendrocyte.

(B and C) The gene ontology categories of the m^{6}A-marked transcripts that belong to OPCs (B) and oligodendrocytes (C) ($\log_2$ |CPM| > 1, *Z* score > 0).

(D) Of the 11,502 transcripts that are expressed in both OPCs and oligodendrocytes, 2,806 transcripts bear the m^{6}A mark in OPCs, but not in oligodendrocytes ($\log_2$ |CPM| > 1, *Z* score > 0).

(E) Of the 11,502 transcripts that are expressed in both OPCs and oligodendrocytes, 1,626 transcripts bear the m^{6}A mark in oligodendrocytes, but not in OPCs.

(F) Of the 11,502 transcripts that are expressed in both OPCs and oligodendrocytes, 23 transcripts bear the m^{6}A mark in both OPCs and oligodendrocytes.

(G) Mouse lines generated for this study. *Mettl14*$^{fl/fl}$ mouse line was crossed with *Olig2*-Cre and *CNP*-Cre mouse lines to conditionally eliminate *Mettl14* in oligodendrocyte lineage cells and postmitotic cells, respectively.

During early development, Olig2+ pMN progenitors produce both motor neurons and oligodendrocytes (Ravanelli and Appel, 2015). Therefore, we explored whether the *Mettl14* deletion affects motor neuron development. We used choline acetyltransferase (ChAT) immunohistochemistry to identify motor neurons in the lumbar spinal cord at P12 and found no difference in motor neuron numbers in both *Mettl14*$^{fl/fl}$*;Olig2*-Cre (Figures S7A, S7B, and S7E) and *Mettl14*$^{fl/fl}$*;CNP*-Cre (Figures S7C, S7D, and S7F) mutant mice compared to controls. In addition, motor neurons express METTL14 in the mutants of both strains (Figures S7B and S7D), suggesting that Cre recombination has a limited effect in motor neurons.

To identify the oligodendrocyte lineage stage(s) that was affected by *Mettl14* inactivation, we examined the number of OPCs and postmitotic oligodendrocytes in P18 *Mettl14*$^{fl/fl}$*;Olig2*-Cre and *Mettl14*$^{fl/fl}$*;CNP*-Cre corpus callosum. CC1 antibody immunostaining specific for mature oligodendrocytes showed that the mutants had significantly fewer mature oligodendrocytes as compared to controls in the corpus callosum of both *Mettl14*$^{fl/fl}$*;Olig2*-Cre (Figures 2E and 2G) and *Mettl14*$^{fl/fl}$*;CNP*-Cre (Figures S1E and S1G) mice. Interestingly, the number of cells positive for PDGF-receptor-alpha (PDGFR-α), a marker for OPCs, showed no difference in the mutants in both *Mettl14*$^{fl/fl}$*;Olig2*-Cre (Figures 2F and 2H) and *Mettl14*$^{fl/fl}$*;CNP*-Cre (Figures S1F and S1H) mice, indicating that the loss of *Mettl14* does not disrupt OPC formation.

To investigate *Mettl14*'s role in OPC proliferation, we co-stained CNS tissue sections with Ki-67, a marker of cellular proliferation, and PDGFR-α to detect OPCs. We found no significant difference in the numbers of proliferating OPCs between mutants and controls in both P18 *Mettl14*$^{fl/fl}$*;Olig2*-Cre (Figures 2F and 2I) and P18 *Mettl14*$^{fl/fl}$*;CNP*-Cre (Figures S1F and S1I) mice. We further examined the effects of *Mettl14* ablation on OPCs and proliferating OPCs at the earlier time point P12, when a larger percentage of OPCs are normally proliferative compared to P18. The quantitative analysis of P12 sections revealed results similar to those seen at P18, with no significant difference of OPC and proliferating OPC numbers between mutants and controls in both *Mettl14*$^{fl/fl}$*;Olig2*-Cre (Figures S6C, S6D, S6K, and S6M) and *Mettl14*$^{fl/fl}$*;CNP*-Cre (Figures S6G, S6H, S6L, and S6N) mice. In addition, similar to P18 mutants, both P12 *Mettl14*$^{fl/fl}$*;Olig2*-Cre (Figures S6A, S6B, and S6I) and *Mettl14*$^{fl/fl}$*;CNP*-Cre (Figures S6E, S6F, and S6J) mice showed reduced numbers of CC1$^+$ mature oligodendrocytes in the corpus callosum.

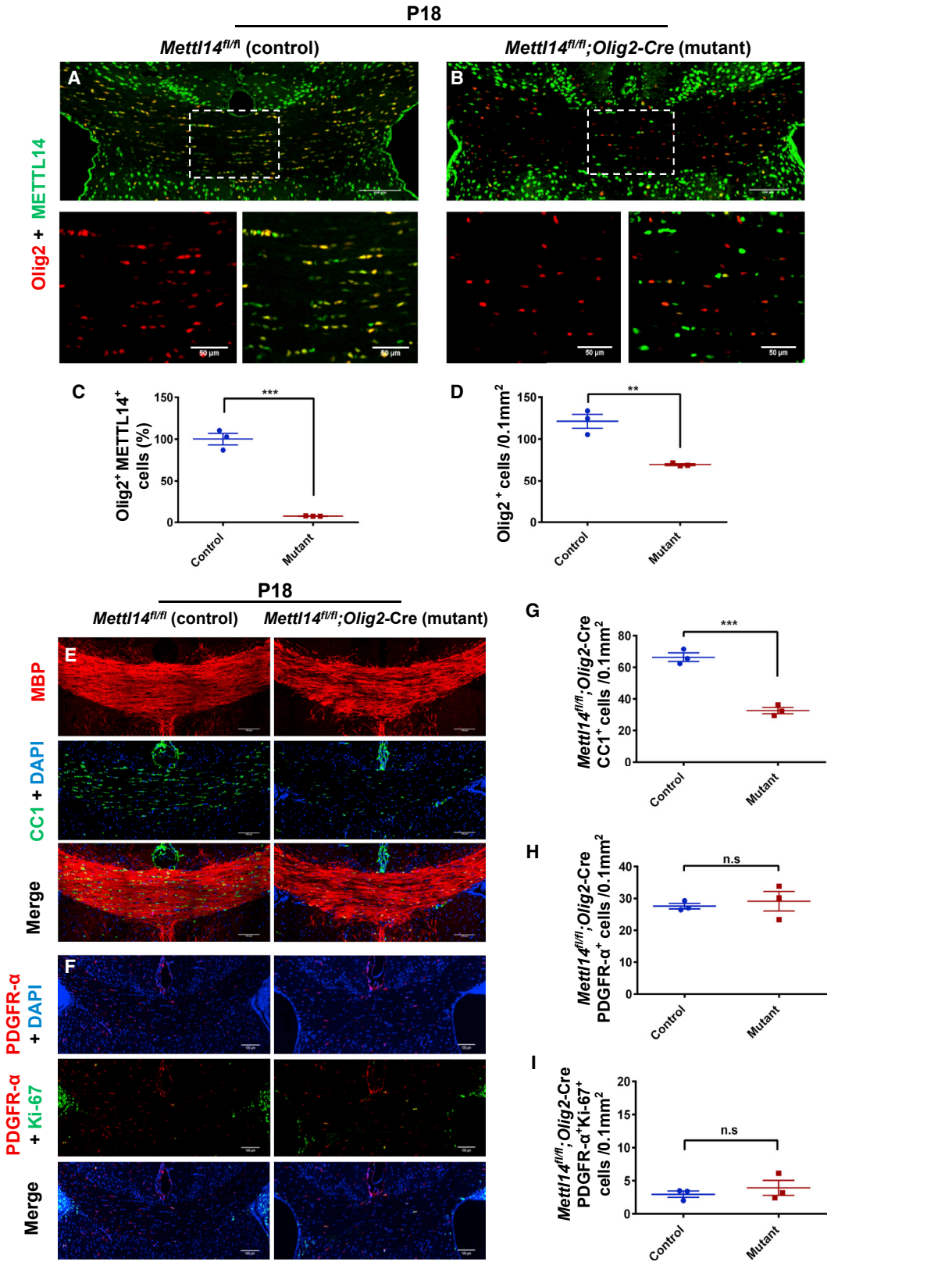

(legend on next page)

Together, our findings demonstrate that *Mettl14* ablation leads to the reduction of oligodendrocyte lineage cells in which mature oligodendrocyte numbers, as opposed to OPC numbers, are predominantly affected.

Mettl14 Ablation in Oligodendrocyte Lineage Cells Leads to Hypomyelination

To characterize the pathological consequences caused by *Mettl14* ablation during myelin development, we examined two different CNS regions, the corpus callosum and optic nerve, in both P18 *Mettl14*$^{fl/fl}$*;Olig2*-Cre and *Mettl14*$^{fl/fl}$*;CNP*-Cre mice using electron microscopy (EM). We found hypomyelination in both corpus callosum and optic nerve in *Mettl14*$^{fl/fl}$*;Olig2*-Cre (Figure 3A) and *Mettl14*$^{fl/fl}$*;CNP*-Cre (Figure S2A) P18 mutants, indicating that pathological changes start when myelin is developing. Quantitative analyses showed significantly increased g ratios, the ratio between the inner axonal and outer total diameter of the myelin sheath, of myelinated axons (Figures 3B and S2B) and a significantly increased percentage of unmyelinated axons in both P18 *Mettl14*$^{fl/fl}$*;Olig2*-Cre (corpus callosum: Figure 3D; optic nerve: Figure 3E) and *Mettl14*$^{fl/fl}$*;CNP*-Cre (corpus callosum: Figure S2D; optic nerve: Figure S2E) mutants. These results revealed decreased thickness of the myelin sheath and fewer myelinated axons upon *Mettl14* ablation. CNS hypomyelination was further supported by western blot analysis, which revealed significant reductions of the myelin proteins MBP and myelin-associated glycoprotein (MAG) expression levels in the *Mettl14*$^{fl/fl}$*;Olig2*-Cre (Figures 3H and 3I) and *Mettl14*$^{fl/fl}$*;CNP*-Cre (Figures S2H and S2I) P18 mutant brains.

To explore whether the pathological change caused by *Mettl14* ablation persists in adulthood, we analyzed adult CNS regions using EM. The *Mettl14*$^{fl/fl}$*;Olig2*-Cre mutant animals are clinically normal until about 6 months (P180) of age, when they begin to display occasional hindlimb flexion, slight ataxia, and mild tremor. The *Mettl14*$^{fl/fl}$*;CNP*-Cre mutant animals start to display tremor and hindlimb clenching at around 4 months of age, with symptoms becoming progressively worse (e.g., ataxic phenotype). The earlier appearance of clinical symptoms in the *Mettl14*$^{fl/fl}$*;CNP*-Cre mutant animals is likely the result of Cre expression in Schwann cells in the peripheral nervous system of the CNP-Cre mice (Brockschnieder et al., 2004). Similar to P18 animals, both *Mettl14*$^{fl/fl}$*;Olig2*-Cre (P180) and *Mettl14*$^{fl/fl}$*;CNP*-Cre (P150) adult mutants displayed myelin abnormalities (Figures 3A and S2A), with increased g ratios (Figure 3C) and non-myelinated axon percentages in both corpus callosum (Figures 3F and S2F) and optic nerve (Figures 3G and S2G). Western blot analysis also revealed decreased myelin protein levels in both P180 *Mettl14*$^{fl/fl}$*;Olig2*-Cre (Figures 3H and 3J) and P150 *Mettl14*$^{fl/fl}$*;CNP*-Cre (Figures S2H and S2J) mutants. Together, our results demonstrate that *Mettl14* is important in CNS myelination.

Mettl14 Ablation Prevents Oligodendrocyte Differentiation

To further determine the role of *Mettl14* in different oligodendrocyte lineage stages, we turned to *in vitro* cultures. We found that the *Mettl14* mutant OPCs were isolated as efficiently as control OPCs and that the mutant cells displayed similar mitotic activity and bipolar morphology in the presence of PDGF-AA (Figures 4A and 4B). Interestingly, the *Mettl14*-deleted cells did not develop into MBP$^+$ mature oligodendrocytes after 5 days of differentiation following removal of PDGF-AA from the culture media (Figure 4D). The mutant cells did not send out the extensive membrane structure seen with control oligodendrocytes (Figure 4C). Indeed, only rare cells (less than 7%; data not shown) that escaped Cre recombination and were METTL14$^+$ in the mutant cell cultures developed into MBP$^+$ cells (Figure 4E). Our western blot data confirmed the almost complete elimination of METTL14 in the mutant oligodendrocytes, as well as the dramatic reduction of major myelin protein (MAG and MBP) expression (Figures 4F and 4G). These results correlate with our *in vivo* findings, strongly suggesting that *Mettl14* is critical for oligodendrocyte maturation.

We next examined cell morphology and maturation from early to late postmitotic differentiation stages of oligodendrocytes *in vitro* to further explore the effects of Mettl14 on oligodendrocyte lineage cell maturation. We used O1, an antibody specific for the myelin galactolipid galactocerebroside, to detect oligodendrocyte morphology (Sommer and Schachner, 1981) from day 1 to day 5 after cells were plated in differentiation media. Interestingly, *Mettl14*-deleted cells (Figure 5C) showed O1 immunoreactivity but did not display the morphological changes

Figure 2. Oligodendrocyte-Lineage-Cell-Specific Ablation of *Mettl14* Results in Loss of Oligodendrocytes

(A and B) Representative METTL14 (green) and Olig2 (red) immunostaining in the corpus callosum of P18 *Mettl14*$^{fl/fl}$*;Olig2*-Cre control (A) and mutant (B) mice (scale bars, 100 μm, 50 μm).

(C) Quantification analysis showing a significantly reduced percentage of Olig2$^+$/METTL14$^+$ double-positive cells in the mutants. Values represent mean ± SEM (n = 3; ***p < 0.001; unpaired Student's t test).

(D) Quantification analysis showing a statistically significant reduction of total oligodendrocyte lineage cells (Olig2$^+$ cells). Values represent mean ± SEM (n = 3; **p < 0.01; unpaired Student's t test).

(E) Representative CC1 (green) and MBP (red) immunostaining in the corpus callosum of P18 *Mettl14*$^{fl/fl}$*;Olig2*-Cre control and mutant mice. Mutant corpus callosum showed visible reduction of oligodendrocytes (CC1$^+$ cells) and patchy myelin (MBP) (scale bar, 100 μm).

(F) Representative PDGFR-α (red) and Ki-67 (green) immunostaining in the corpus callosum of P18 *Mettl14*$^{fl/fl}$*;Olig2*-Cre control and mutant mice (scale bar, 100 μm).

(G) Quantification showing a significant reduction of CC1$^+$ cells (OLs) in P18 *Mettl14*$^{fl/fl}$*;Olig2*-Cre mutant corpus callosum. Values represent mean ± SEM (n = 3; ***p < 0.001; unpaired Student's t test).

(H) Quantification showing no significant difference between control and mutant numbers of PDGFR-α$^+$ cells (OPCs) in P18 *Mettl14*$^{fl/fl}$*;Olig2*-Cre mice. Values represent mean ± SEM (n = 3; p > 0.05; unpaired Student's t test).

(I) Quantification showing no significant difference between control and mutant numbers of PDGFR-α$^+$ and Ki67$^+$ double-positive cells in P18 *Mettl14*$^{fl/fl}$*;Olig2*-Cre mice. Values represent mean ± SEM (n = 3; p > 0.05; unpaired Student's t test).

See also Figures S1 and S5–S7.

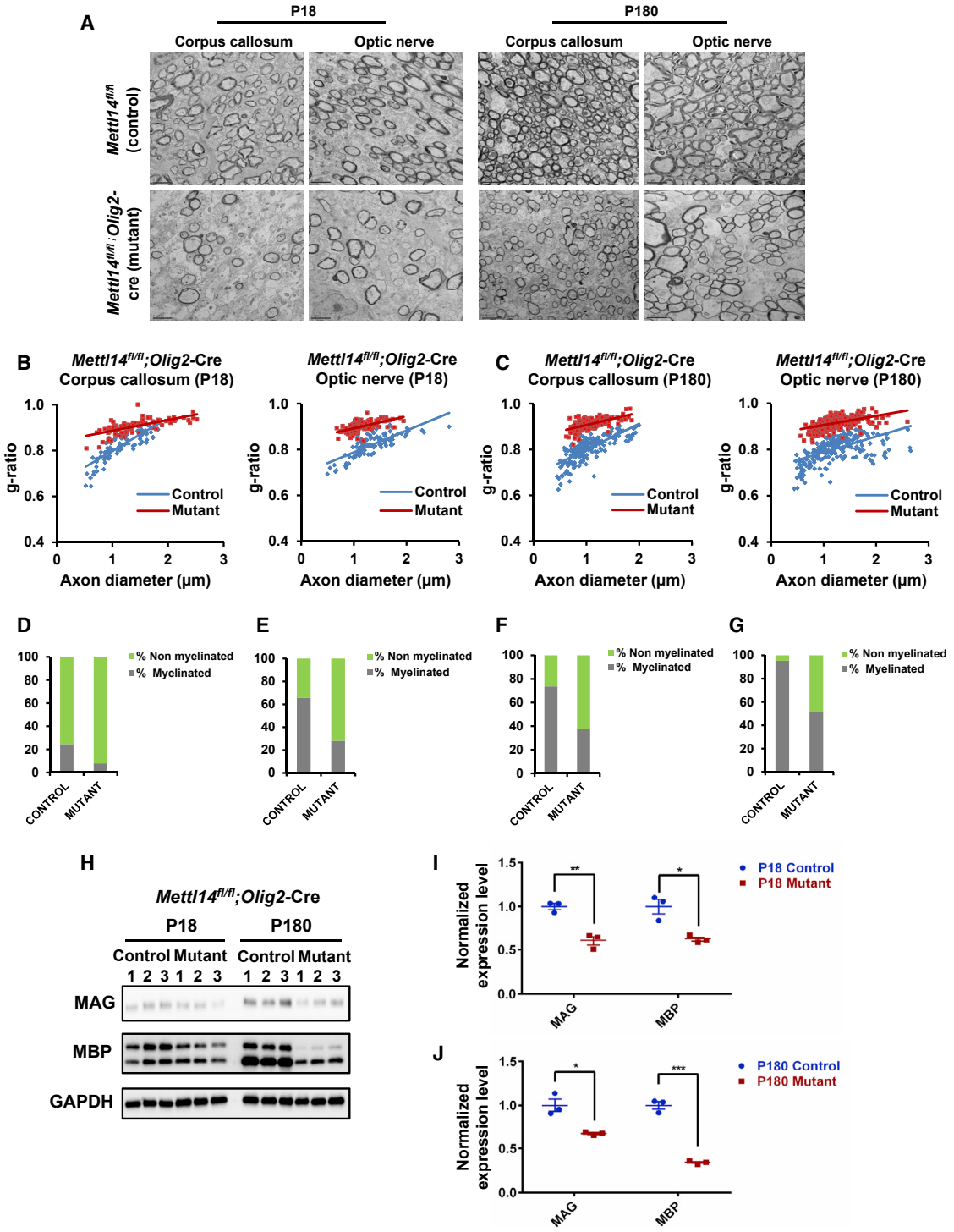

Figure 3. *Mettl14* Ablation Leads to Hypomyelination

(A) Representative EM images of corpus callosum and optic nerve in P18 and P180 *Mettl14*$^{fl/fl}$;*Olig2*-Cre control and mutant animals. Mutant corpus callosum and optic nerve had thinner myelin and fewer myelinated axons in both ages (scale bar, 2 μm).

(B) g ratio analyses showing significantly higher g ratios in both P18 *Mettl14*$^{fl/fl}$;*Olig2*-Cre mutant corpus callosum (mutant g ratio = 0.91, control g ratio = 0.80) and optic nerve (mutant g ratio = 0.90, control g ratio = 0.82) (n = 3; ***p < 0.001; unpaired Student's t test).

(C) g ratio analyses showing significantly higher g ratios in both P180 *Mettl14*$^{fl/fl}$;*Olig2*-Cre mutant corpus callosum (mutant g ratio = 0.91, control g ratio = 0.80) and optic nerve (mutant g ratio = 0.91, control g ratio = 0.83) (n = 3; ***p < 0.001; unpaired Student's t test).

(legend continued on next page)

of control cells, which progressively extended their membrane structures to form complex membrane sheets (Figure 5A). The *Mettl14*-ablated cells did not express appreciable levels of MBP (Figure 5D), whereas control cells matured gradually from day 1 to day 5 with increasing MBP expression (Figure 5B). These results, together with our *in vivo* data, strongly suggest that *Mettl14* plays an important role in postmitotic oligodendrocyte maturation.

Mettl14 Ablation Differentially Alters the OPC and Oligodendrocyte Transcriptomes

To elucidate the effects of *Mettl14* on oligodendrocyte lineage cell gene expression during development at the transcriptome level, we performed RNA-seq with both purified OPCs and cultured mature oligodendrocytes from *Mettl14*$^{fl/fl}$;*Olig2*-Cre control and mutant mice. The quantification of differential expression in the *Mettl14* mutant transcriptome revealed distinct differences in the OPCs and myelinating oligodendrocytes. For quantification analysis, we defined the significance of differentially expressed transcripts using the following three criteria: (1) a 99.9% confidence interval, adjusted for false discovery, as a q value using methods previously described (Benjamini and Yekutieli, 2005); (2) fold changes (FCs) that exceeded 2.0-fold ($\log_2$ |FC| > 1) in expression; and (3) an expression level that exceeded two counted transcripts per million ($\log_2$ |CPM| > 1). Of the 11,809 transcripts present in the OPC transcriptome, 586 were expressed at significantly higher levels and 177 were expressed at significantly lower levels in the mutant cells (Figure 6A). Among the 12,542 transcripts present in mature oligodendrocytes, 1,388 transcripts were significantly upregulated and 1,247 were downregulated in the mutant cells (Figure 6B). Interestingly, among the significantly downregulated oligodendrocyte transcripts, many are normally highly expressed in myelinating oligodendrocytes, such as *Mbp*, *Mog*, *Mag*, *Plp1*, and *Cnp* (Figure 6B). The downregulation of these myelin transcripts correlates with the downregulation of myelin protein expression observed in the *Mettl14*-ablated mutant animals.

The m^{6}A mark has been shown to play a role in reducing the stability of m^{6}A-containing transcripts (Wang et al., 2014, 2018; Weng et al., 2018a; Yoon et al., 2017; Zhang et al., 2017). Accordingly, many transcripts in the *Mettl14*$^{fl/fl}$;*Olig2*-Cre mutants had higher relative expression levels. We compared the m^{6}A-seq data and RNA-seq data and found that, among the 3,554 m^{6}A-marked OPC transcripts, 46 transcripts had significantly downregulated expression levels and 108 transcripts had significantly upregulated expression levels (Figure 6C). Among the 2,606 m^{6}A-marked oligodendrocyte transcripts, 221 had significantly downregulated expression levels and 217 transcripts had significantly upregulated expression levels (Figure 6D). Gene ontology analysis of significantly altered m^{6}A-marked transcripts revealed many important functions such as glia cell development in OPCs (Figure 6E) and myelination in oligodendrocytes (Figure 6F). These results indicate that the m^{6}A mark differentially regulates the OPC and oligodendrocyte transcriptomes.

Mettl14 Regulates OPC and Oligodendrocyte Transcripts that Are Critical for Oligodendrocyte Lineage Progression

In order to find clues of how the m^{6}A mark regulates oligodendrocyte lineage development, we examined the expression of factors that play a critical cell-autonomous role in oligodendrocyte lineage progression by cross-comparing our m^{6}A-seq and RNA-seq datasets. We identified a number of transcripts that encode transcriptional factors implicated in oligodendrocyte lineage progression as being dynamically marked by m^{6}A at different oligodendrocyte lineage stages. For example, *Hey1*, *Klf19*, *Sox2*, *Sox5*, *Srebf1*, *Tcf19*, and *Zeb2* are marked by m^{6}A in OPCs, but not in oligodendrocytes; *Hes1*, *Nkx6.2*, *Olig2*, and *Yy1* are marked by m^{6}A only in oligodendrocytes, but not in OPCs (Table S1). The dynamic m^{6}A-marked status of these transcription factor transcripts suggests a time-specific, post-transcriptional regulatory role of m^{6}A during oligodendrocyte lineage progression and may contribute to the differentially altered transcriptome in OPCs and oligodendrocytes following *Mettl14* deletion.

Studies have shown that DNA epigenetic regulation mechanisms, such as chromatin remodeling and histone modifications, are important for oligodendrocyte lineage progression (Koreman et al., 2018). Our RNA-seq and m^{6}A-seq analyses revealed that many transcripts encoding histone modification regulators bear an m^{6}A mark and were significantly differentially expressed in the mutant transcriptome (Table S2). We detected transcripts of histone "writers" such as histone acetyltransferases (HATs) *Hat1*; histone methyltransferases (HMTs) *Smyd2*, *Prdm2*, *Setdb1*, *Suv39 h1*, *Ash1l*, and *Dot1l*; histone "erasers" such as histone deacetylases (HDACs) *Hdac3*, *Hdac7*, *Hdac8*, *Hdac9*; and lysine demethylases (KDMs) *Kdm2b*, *Kdm5c*, *Kdm3b*, *Kdm4a*, *Kdm4c*, and *Kdm6a* that had the m^{6}A mark and had significantly altered mRNA levels in the *Mettl14*-ablated mutants: these transcripts encode proteins with important regulator functions in oligodendrocyte development (Hernandez and Casaccia, 2015). Thus, our findings suggest a possible link between m^{6}A RNA modification and histone modifications in the regulation of oligodendrocyte lineage development.

We also examined key signaling pathways that are critically involved in oligodendrocyte lineage progression. We found transcripts that were significantly altered by *Mettl14* ablation in the BMPs, ERK/MAPK, fibroblast growth factor families (FGFs), Notch/Delta, and Shh and Wnt signaling pathways in OPCs (Table S3) and P13K/AKT/mTOR, BMPs, ERK/MAPK, insulin-like growth factor-1 (IGF-1), Notch/Delta, and Shh and Wnt signaling pathways in oligodendrocytes (Table S4). The alternation of

(D–G) Percentage of myelinated axons in corpus callosum and optic nerve (D: P18 *Mettl14*$^{fl/fl}$;*Olig2*-Cre corpus callosum; E: P18 *Mettl14*$^{fl/fl}$;*Olig2*-Cre optic nerve; F: P180 *Mettl14*$^{fl/fl}$;*Olig2*-Cre corpus callosum; G: P180 *Mettl14*$^{fl/fl}$;*Olig2*-Cre optic nerve) (n = 3, ***p < 0.001; unpaired Student's t test).

(H) Western blot showing myelin protein expression (MAG, MBP) levels in both P18 and P180 *Mettl14*$^{fl/fl}$;*Olig2*-Cre control and mutant animals (n = 3).

(I and J) Quantification of immunoblots. MAG and MBP expression levels were normalized to GAPDH expression levels. Both MAG and MBP were significantly reduced in P18 (I) and P180 (J) *Mettl14*$^{fl/fl}$;*Olig2*-Cre mutants. Values represent mean ± SEM (n = 3; *p < 0.05; ***p < 0.01; ***p < 0.001; unpaired Student's t test). See also Figure S2.

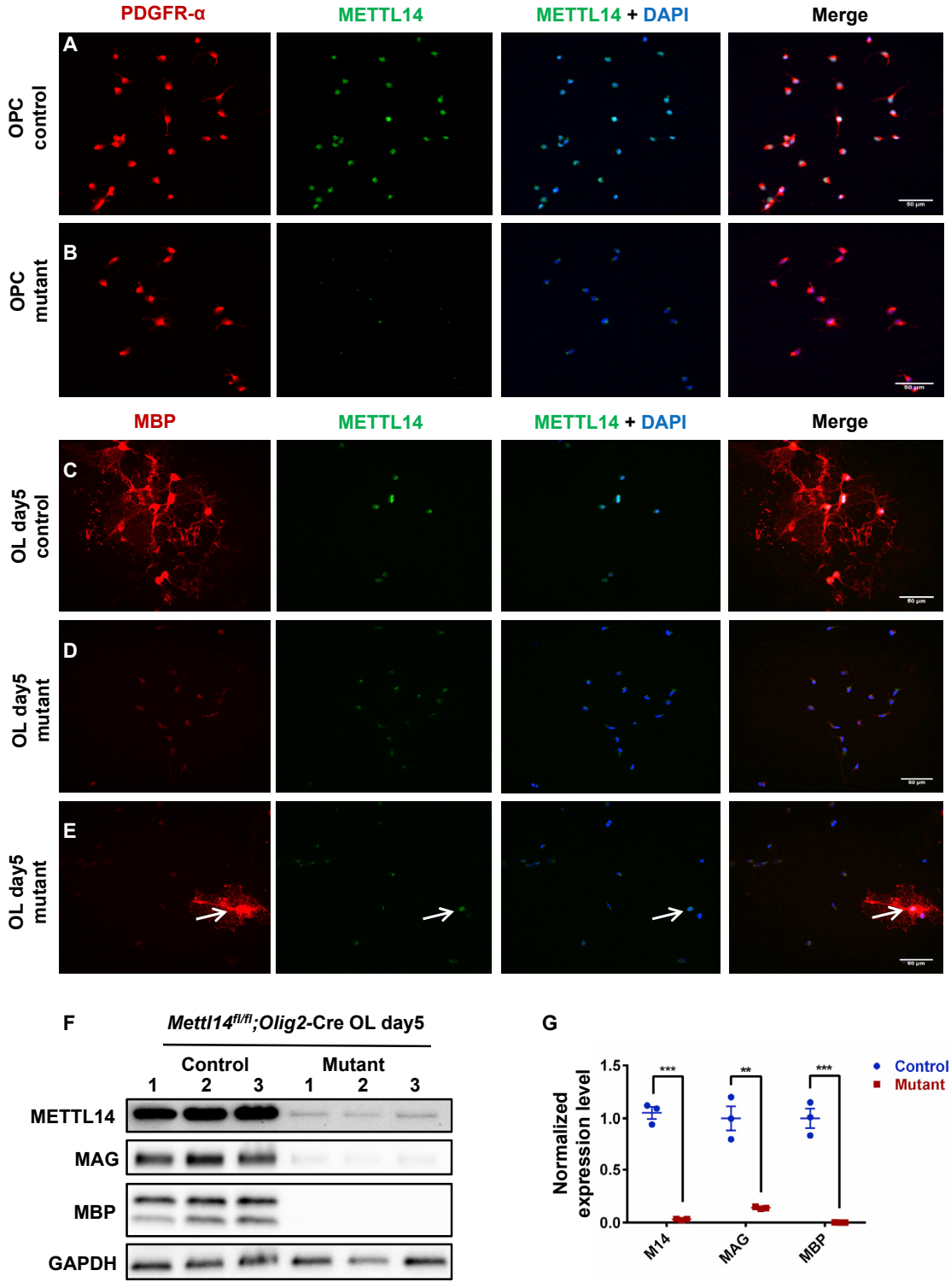

Figure 4. *Mettl14*-Ablated OPCs Fail to Develop into Mature Oligodendrocytes *In Vitro*

(A and B) PDGFR-α and METTL14 immunostaining of *Mettl14*$^{fl/fl}$;*Olig2*-Cre control (A) and mutant (B) OPCs in culture. METTL14 was eliminated from the mutant OPCs, which showed no morphological changes compared to control OPCs (scale bar, 50 μm).

(C and D) MBP and METTL14 immunostaining of *Mettl14*$^{fl/fl}$;*Olig2*-Cre control (C) and mutant (D) oligodendrocytes that had been cultured in differentiation media for 5 days (oligodendrocyte day5). Mutant cells fail to develop into MBP-positive cells (scale bar, 50 μm).

(legend continued on next page)

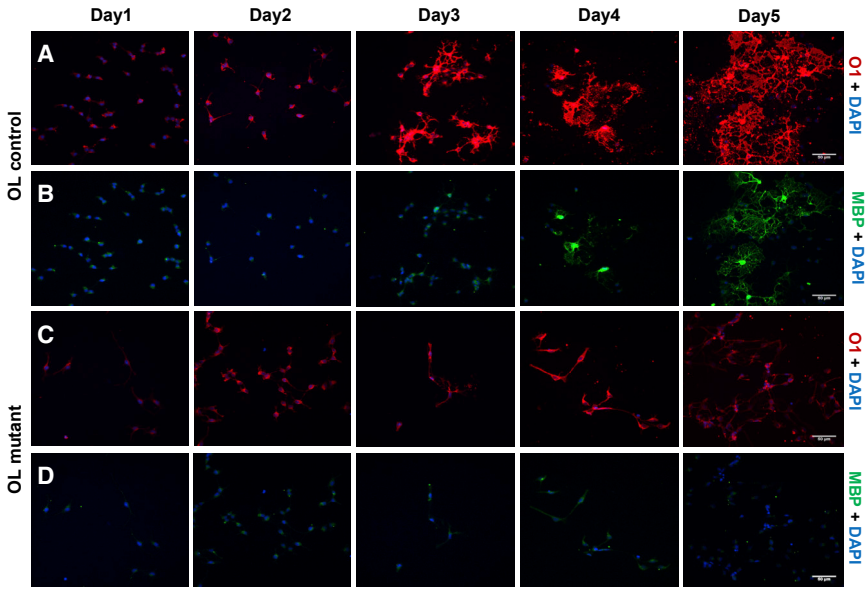

Figure 5. *Mettl14* Ablation Prevents Oligodendrocyte Differentiation

(A and B) O1 (A) and MBP (B) immunostaining of *Mettl14*$^{fl/fl}$ (control) oligodendrocytes that had been seeded in differentiation media for 1–5 days (day1–5). Control cells progressively differentiated into mature oligodendrocytes (scale bar, 50 μm). (C and D) O1 (C) and MBP (D) immunostaining of *Mettl14*$^{fl/fl}$*;Olig2*-Cre (mutant) oligodendrocytes that had been seeded in differentiation media for 1–5 days (day1–5). Mutant cells did not differentiate into MBP-positive oligodendrocytes and never formed membrane sheath structures like control cells (scale bar, 50 μm).

critical gene expression levels in these signaling pathways provided us with important clues regarding disruption of oligodendrocyte maturation displayed by the *Mettl14*$^{fl/fl}$*;Olig2*-Cre and *Mettl14*$^{fl/fl}$*;CNP*-Cre animals. Indeed, many transcripts that encode critical components of these signaling pathways have the m^{6}A mark (Figure 6G; Tables S3 and S4), suggesting that m^{6}A may regulate these signaling pathways to promote oligodendrocyte lineage progression.

Mettl14's Possible Mechanism of Actions in Oligodendrocyte Lineage Cells

We also wished to explore potential mechanism(s) of action of the m^{6}A mark in regulating oligodendrocyte lineage cell development and function in addition to the disruption of the cells' transcriptomes discussed above. Previous studies have shown m^{6}A's role in increasing the translational efficiency of the marked transcripts in various systems (Coots et al., 2017; Shi et al., 2017; Wang et al., 2015; Zhou et al., 2018). In order to investigate this potential mechanism, we compared transcriptional and translational levels of a subset of the m^{6}A-marked transcripts that encode proteins critical for oligodendrocyte development (Bujalka et al., 2013; Zhou and Anderson, 2002). We found significantly decreased levels of these proteins both *in vivo* (Figures 3H–3J) and *in vitro* (Figures 4F, 4G, S8A, and S8B); however, the observed reductions correlated with the levels of mRNA reduction found in the oligodendrocyte transcriptome (Table S5), suggesting that translational regulation may not be a key feature of m^{6}A gene regulation in oligodendrocyte lineage cells. Nevertheless, a more comprehensive proteomics assessment will be required to determine the global impact of the m^{6}A mark on translational efficiency in oligodendrocytes.

MBP, a predominant and critical protein of myelin, is translated locally in the myelin compartment (Colman et al., 1982), which requires the active transport of its mRNA into oligodendrocyte processes (Carson et al., 1997). This transport requires the RNA-binding protein heterogeneous nuclear ribonucleoprotein (hnRNP) A2 (Hoek et al., 1998; Müller et al., 2013). Importantly, it was recently discovered that hnRNPA2B1, an isoform of hnRNPA2 that is expressed in oligodendrocyte lineage cells (Han et al., 2010), is an m^{6}A reader (Alarcón et al., 2015), suggesting that the m^{6}A mark might have a role in regulating *Mbp* mRNA transport in oligodendrocytes. In order to investigate this possibility, we used the RNAscope approach to determine the distribution of *Mbp* and *Myrf* mRNA in oligodendrocytes of the corpus callosum. In controls, *Myrf* mRNA is localized in the oligodendrocyte cell bodies, whereas *Mbp* mRNA distributes to the complex, web-like oligodendrocyte processes (Figure S3A). In P18 *Mettl14*$^{fl/fl}$*;Olig2*-Cre mutant oligodendrocytes, *Myrf* and *Mbp* mRNA levels are clearly reduced (Figure S3B), as expected, but the distribution of these transcripts does not appear altered, suggesting that the absence of the m^{6}A mark has not disrupted the transport of the *Mbp* mRNA into the myelin compartment. In addition to MBP mRNA, a number of key oligodendrocyte transcripts have been shown to be localized in the myelin sheath (Thakurela et al., 2016). A more extensive analysis of the myelin mRNA content of the *Mettl14* mutants will help determine the role of the m^{6}A mark in the establishment of myelin transcriptome.

Functional variant isoforms of myelin proteins are generated by alternative splicing to ensure precise oligodendrocyte lineage progression (Montague et al., 2006; Zhang et al., 2014; Zhao et al., 2010a). Previous studies have shown that m^{6}A plays a critical role in regulating mRNA splicing in various cellular systems (Haussmann et al., 2016; Xiao et al., 2016; Zhao et al., 2014;

(E) Only rare cells (white arrow pointed) that had escaped Cre-mediated recombination and thus expressed METTL14 in the mutant day5 OL group successfully differentiated into MBP-expressing oligodendrocytes (scale bar, 50 μm).

(F) Western blot showing METTL14, MAG, MBP, and GAPDH expression levels in control and mutant OL day5 groups.

(G) Quantification of immunoblots showing significant reduction of METTL14, MAG, and MBP expression in mutant OL day5 group. METTL14, MAG, and MBP expression levels were normalized to GAPDH expression level. Values represent mean ± SEM (n = 3; **p < 0.01; ***p < 0.001, unpaired Student's t test).

See also Figure S4.

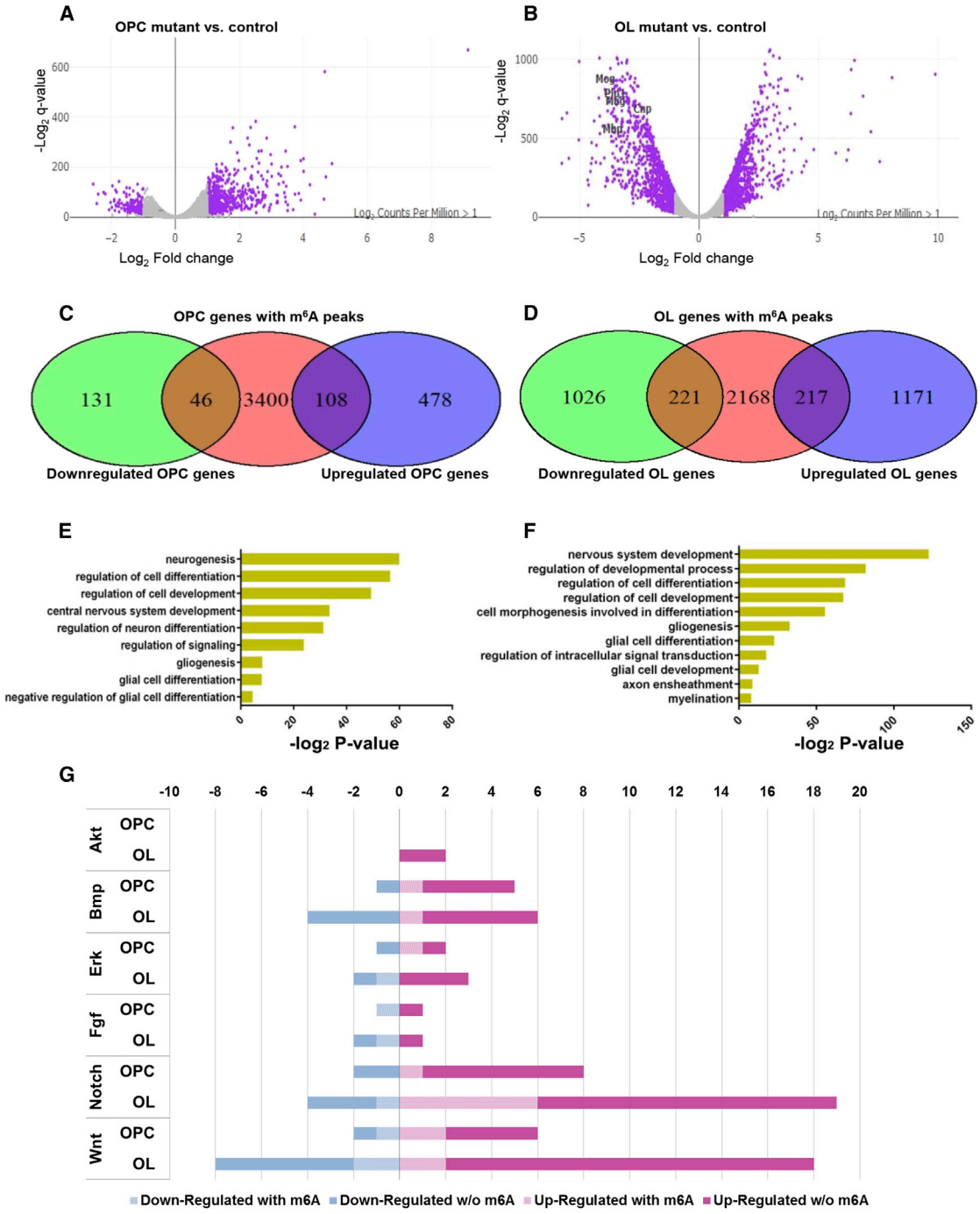

Figure 6. *Mettl14* Deletion Differentially Alters OL and OPC Transcriptome

(A and B) Volcano plots display the differentially expressed genes in the *Mettl14*$^{fl/fl}$;*Olig2*-Cre OPC (A) and oligodendrocyte (B) mutants versus controls (n = 3). The highlighted genes (purple) are significantly (q value < 0.001, $\log_2$ |CPM| > 1) regulated and have a notable fold change ($\log_2$ |FC| > 1) in their expression in the mutants. Selected myelin genes are labeled.

(C and D) Venn diagram shows the numbers of significantly downregulated or upregulated OPC (C) and oligodendrocyte (OL) (D) transcripts that also have the m^{6}A mark.

(E and F) The ontology categories of the m^{6}A-marked transcripts that are significantly altered in the OPCs (E) and oligodendrocytes (F) ($\log_2$ |FC| > 1, $\log_2$ |CPM| > 1, q value < 0.001, *Z* score > 0).

(G) Bar graph shows the number of m^{6}A-marked transcripts in the selected altered signaling pathways in OPCs and oligodendrocytes ($\log_2$ |FC| > 1, $\log_2$ |CPM| > 1, q value < 0.001, *Z* score > 0).

See also Figure S8 and Tables S1–S5.

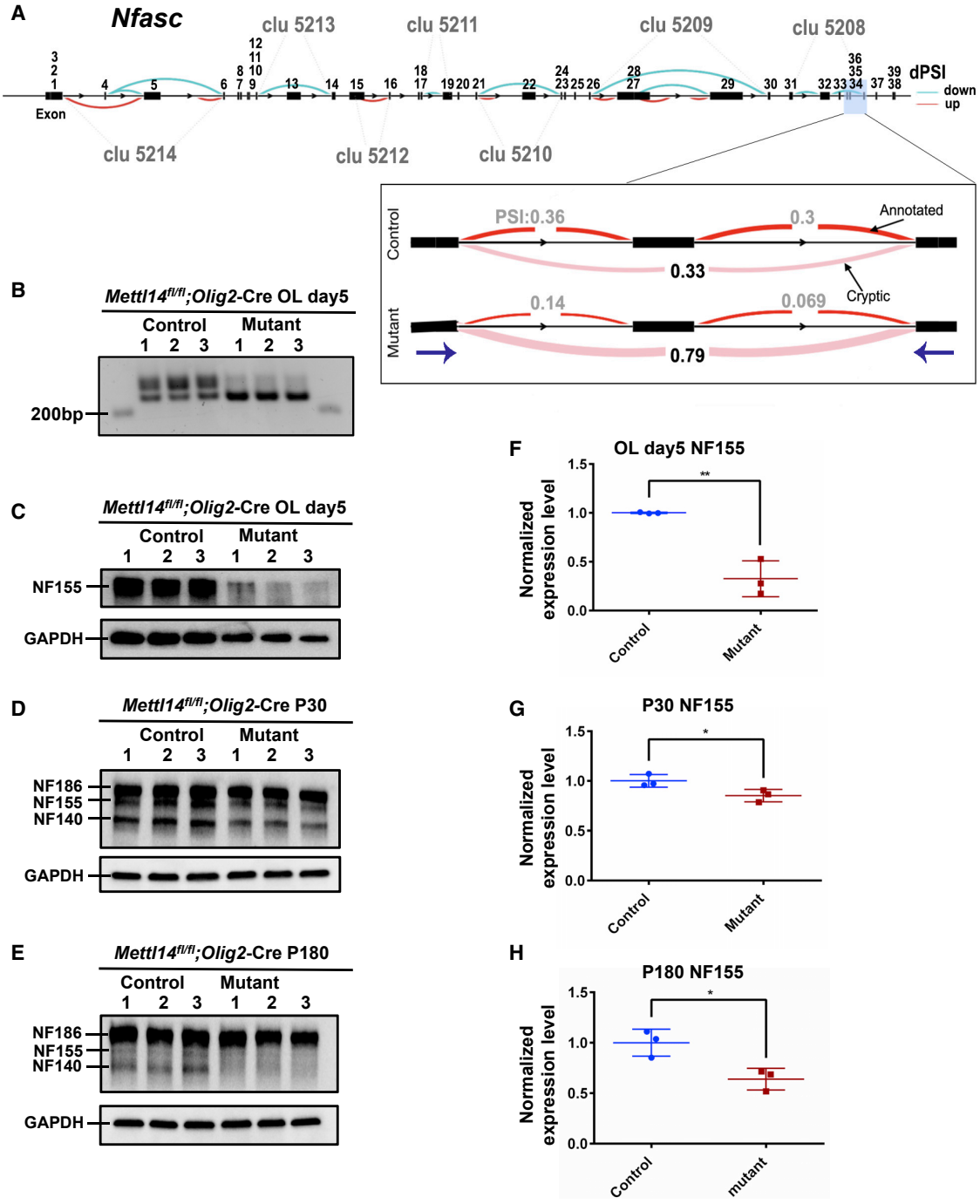

Figure 7. *Mettl14* Deletion Differentially Alters *Nfasc155* Alternative Splicing and Expression

(A) Schematic view of differentially spliced sites in the *Nfasc* gene in control versus *Mettl14*$^{fl/fl}$;*Olig2*-Cre mutant day5 oligodendrocytes. The 39 *Nfasc* exons are labeled above the exons. Each cluster (i.e., abbreviated as "clu X") represents a group of introns that display alternative excision events. Specifically, these are introns that share a donor site (canonical 5′ splice site, AT) or acceptor site (canonical 3′ splice site, GA). Blue curves represent cases that have fewer splicing events in the mutants, while the red curves represent cases with more splicing events in the mutants ($p < 0.05$). The magnified window shows the sample cluster (clu 5208) that we examined for the presence of aberrant spliced isoforms in the mutants in (B). Purple arrows represent the start points for reverse and forward primers that we used for RT-PCR in (B).

(B) Differentially spliced *Nfasc* isoforms were detected by RT-PCR and agarose gel electrophoresis in the *Mettl14*$^{fl/fl}$;*Olig2*-Cre day5 oligodendrocyte mutants (218 kb). Primers used: Forward, ACTGGGAAAGCAGATGGTGG; Reverse, ACATGAGCCCGATGAACCAG.

(legend continued on next page)

Zhou et al., 2019). In order to investigate the potential role of the m^{6}A mark in regulating differential splicing during oligodendrocyte development, we used LeafCutter (Li et al., 2018) to identify altered splicing events in OPC and oligodendrocyte transcriptomes. LeafCutter identifies alternatively excised intron clusters and compares differentially excised intron levels between controls and mutants. Differential splicing is measured by changes in the percent spliced in (change, or delta, dPSI) (Li et al., 2018). Global comparison of alternative splicing events revealed numerous statistically significant changes in *Mettl14*-ablated mutants versus controls (Stouffer's Z score = 40.86 in OPCs and 105.76 in oligodendrocytes). In addition, we found that 1,372 splicing events in 364 genes in OPCs and 1,930 splicing events in 485 genes in oligodendrocytes were differentially spliced upon *Mettl14* deletion ($q < 0.01$). A number of significant differentially alternative spliced transcripts were previously shown to encode proteins with important functions in the myelinating process, such as protein tyrosine phosphate receptor type Z1(*Ptprz1*) in OPCs (Harroch et al., 2002) and neurofascin (*Nfasc*) in oligodendrocytes (Tables S6 and S7). Interestingly, the neurofascin protein (NF), which is essential in the establishment and maintenance of node of Ranvier domains (Howell et al., 2006; Pillai et al., 2009; Sherman et al., 2005; Thaxton et al., 2010; Zonta et al., 2008), has the most significantly altered isoforms and bears the highest differential dPSI level in the oligodendrocyte transcriptome (Figure 7A; Table S7).

To further investigate the role of m^{6}A mRNA methylation in regulating the distribution of NF isoforms during development, we used RT-PCR to confirm the differential distribution of distinct splicing products (Figure 7B) in purified oligodendrocyte mRNA from mutants and controls. This analysis confirmed the presence of the predicted altered spliced *Nfasc* mRNA product in the mutant oligodendrocytes. Since NF155 is the glial NF isoform that is required for the assembly of paranodal domains (Sherman et al., 2005), we examined NF155 expression levels in different developmental stages *in vitro* and *in vivo*. *Mettl14$^{fl/fl}$;Olig2*-Cre mutant oligodendrocytes that had been cultured in differentiation media for 5 days had a significant reduction of NF155 expression compared to controls (Figures 7C and 7F). *In vivo*, 1-month-old animals (P30) showed significantly decreased NF155 levels in the *Mettl14$^{fl/fl}$;Olig2*-Cre mutants (Figures 7D and 7G). To further analyze nodal and paranodal domains with immunohistochemistry, we used antibodies to the voltage-gated sodium channel (NaCh) and Caspr to identify the nodal and paranodal domains, respectively (Figures 8A and 8B). We found a significant reduction in the number of nodes at P30 in the mutants compared to controls (Figure 8E). We also used pan-NF antibody to characterize NF localization and morphology in both nodal and paranodal domains (Figures 8A and 8B). We found no difference in node and paranode size in the mutants as compared to controls (Figure 8F).

We further investigated whether NF155 expression abnormalities persist to adulthood (P180) in *Mettl14$^{fl/fl}$;Olig2*-Cre mutants. Western blot results revealed significantly reduced expression levels of NF155 in P180 mutants (Figures 7E and 7H). Next, we measured nodal and paranodal domains via immunohistochemistry in these animals (Figures 8C and 8D). We found a significant reduction of node numbers in the mutants (Figure 8G). In addition, both nodal and paranodal domains showed significantly increased sizes in the mutants (Figure 8H), suggesting widespread pathological changes at the node of Ranvier in adult *Mettl14$^{fl/fl}$;Olig2*-Cre mutants.

DISCUSSION

RNA modifications have recently emerged as critical post-transcriptional regulatory mechanisms to modulate gene expression (Frye et al., 2018). Among all post-transcriptional mRNA modifications, m^{6}A is the most abundant internal alteration found in eukaryotic mRNA (Yue et al., 2015). In contrast to DNA and protein methylation, m^{6}A methylation has the potential to have a very rapid influence on transcriptome changes during cell-state transitions (Frye et al., 2018; Zhao and He, 2017).

In this report, we show that oligodendrocyte lineage progression is accompanied by changes in m^{6}A modification on numerous transcripts. We also show that *Mettl14*, which encodes an essential m^{6}A writer component, is critical in regulating oligodendrocyte development and CNS myelination. We demonstrate altered oligodendrocyte numbers and hypomyelination in both oligodendrocyte-lineage-cell-specific *Mettl14*-ablated mice. Nevertheless, OPC numbers were not altered by *Mettl14* ablation. We also show that *Mettl14*-ablated OPCs lacked the ability to differentiate into mature MBP-positive, myelin-forming oligodendrocytes *in vitro*. These results indicate that the m^{6}A RNA modification is essential for postmitotic oligodendrocyte differentiation.

Interestingly, our data revealed a more severe developmental phenotype *in vitro* than *in vivo*, suggesting that communication with other CNS cell types may mitigate the effects of the *Mettl14* deletion *in vivo*. In addition, it is curious that when we cultured *Mettl14$^{fl/fl}$;CNP*-Cre OPCs (data not shown), in which the *Mettl14* gene is inactivated later in the oligodendrocyte lineage, the mutant cells had the capacity to differentiate into MBP-positive, mature oligodendrocytes as efficiently as control cells, suggesting that the severe block in maturation that occurs in the *Mettl14$^{fl/fl}$;Olig2*-Cre OPCs *in vitro* is the result of an m^{6}A deficiency early in the oligodendrocyte lineage. This is supported by the failure of enforced METTL14 expression in the *Mettl14$^{fl/fl}$;Olig2*-Cre OPCs to fully rescue the severe *in vitro* differentiation phenotype (Figure S4). Our future efforts will be devoted to elucidating the effects of the m^{6}A mark at distinct stages of the oligodendrocyte lineage.

Oligodendrocyte differentiation involves many steps that must be regulated in time and space (Zuchero and Barres, 2013). Our RNA-seq and m^{6}A-seq data revealed changes of the m^{6}A-marked status on numerous transcripts that encode critical

(C–E) Western blot results of NFASC *in vitro* (C) and *in vivo* (D: P30; E: P180).
(F–H) Quantification of NF155 expression *in vitro* (F) and *in vivo* (G: P30; H: P180). NF155 expression level was normalized to GAPDH expression level. NF155 had significant reduction in both P30 and P180 *Mettl14$^{fl/fl}$;Olig2*-Cre mutants. Values represent mean ± SEM (n = 3; *p < 0.05; **p < 0.01; unpaired Student's t test). See also Figure S3 and Tables S6 and S7.

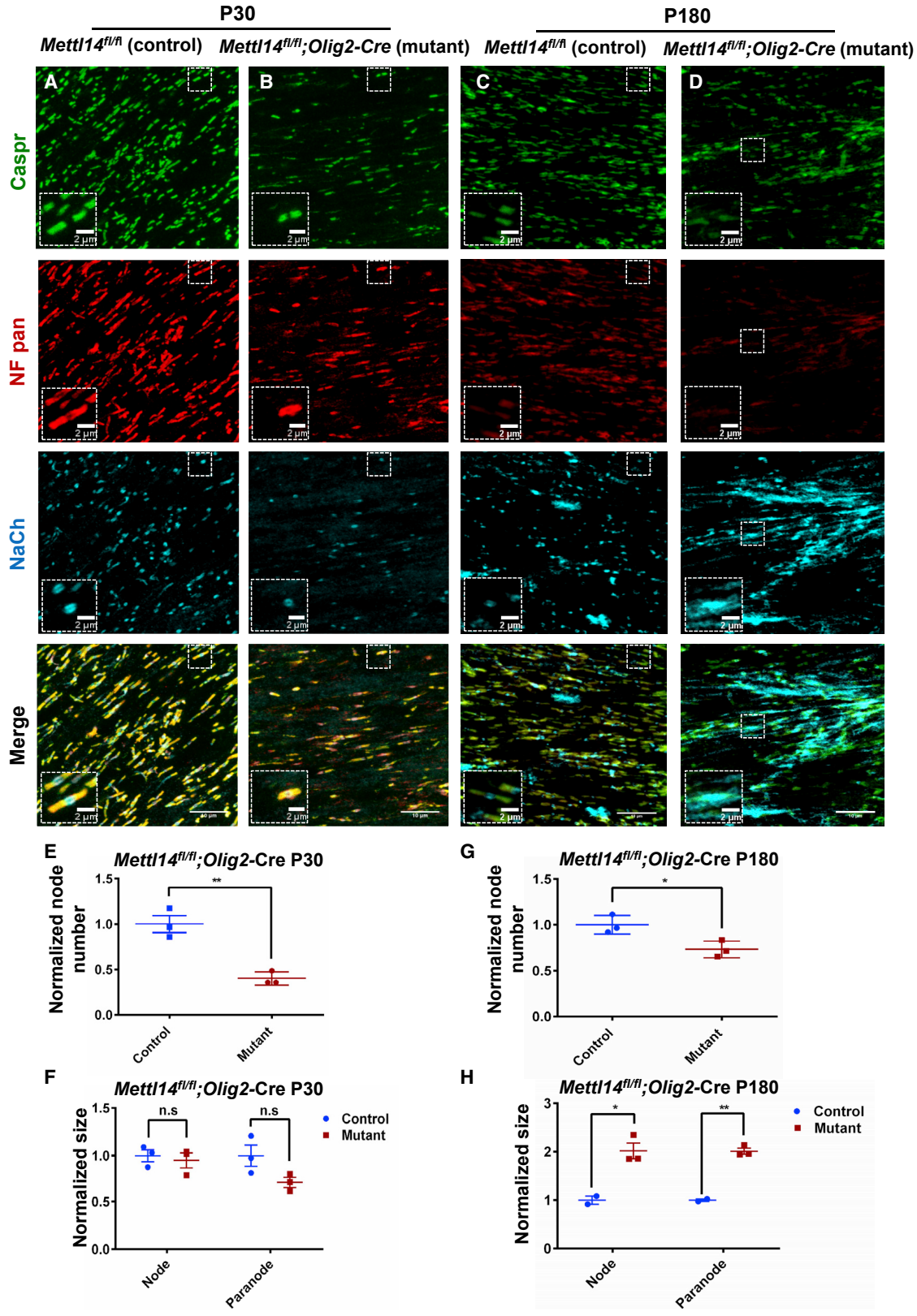

(legend on next page)

transcription factors in OPCs and oligodendrocytes, suggesting that m^{6}A mRNA modification contributes to transcriptional changes during oligodendrocyte development. Indeed, emerging studies have shown that the turnover and/or translation of transcripts during cell-state transitions regulated by the m^{6}A mark represent an important developmental mechanism (Frye et al., 2018).

The functional role of various histone modifiers in oligodendrocyte differentiation is stage dependent, yet the underlying regulatory role of these factors is unknown (Copray et al., 2009; Hernandez and Casaccia, 2015). Our study revealed that transcripts that encode a number of histone modifiers are dynamically marked by m^{6}A in OPCs and oligodendrocytes (Table S2), suggesting that m^{6}A RNA modifications may play a role in regulating the expression of epigenetic modifiers at distinct oligodendrocyte lineage stages. Consistent with this possibility, a recent study revealed cross-talk between m^{6}A RNA modification and histone modification (Wang et al., 2018).

In addition, we also found numerous oligodendrocyte lineage signaling pathway transcripts that are dynamically marked by m^{6}A and expressed at significantly altered levels in the absence of METTL14. The alternation of m^{6}A-marked transcripts is accompanied by significant alterations of other important pathway transcripts that do not bear an m^{6}A mark, suggesting that m^{6}A RNA modification may have a primary or secondary effect on gene expression. Together, our RNA-seq and m^{6}A-seq results indicate that m^{6}A RNA modifications modulate the expression of multiple transcriptional regulators, DNA epigenetic modifiers, and signaling pathways to facilitate oligodendrocyte lineage progression.

In addition to the effect on mRNA levels discussed above, we examined several additional potential functions of the m^{6}A mark on gene expression in oligodendrocyte lineage cells. We explored whether the m^{6}A mark affects translational efficiency of important myelin genes and their regulators because it had previously been shown that translational efficiency of marked transcripts is increased (Shi et al., 2017; Wang et al., 2015). Surprisingly, we did not detect dramatic alternations of protein levels when compared with mRNA levels of m^{6}A-marked transcripts. The m^{6}A mark has also been shown to play a role in intracellular mRNA transport (Roundtree et al., 2017). Therefore, we examined the transport of *Mbp* mRNA into oligodendrocyte processes, which has been shown to be critical for CNS myelination. Nevertheless, using RNAscope, we were unable to detect a significant decrease in the efficiency with which the *Mbp* mRNA is transported into the myelin domain in the *Mettl14* mutant animals. Although these initial efforts did not reveal a role for the m^{6}A mark in mRNA translation or subcellular transport, more thorough analyses may uncover alterations in these processes in the *Mettl14* mutant oligodendrocytes.

We did, however, detect widespread changes in the *Mettl14* mutant oligodendrocyte lineage cells that were related to aberrant RNA splicing. In fact, 283 out of 364 (~78%) aberrantly spliced OPC transcripts and 311 out of 485 (~64%) aberrantly spliced oligodendrocyte transcripts are marked by m^{6}A. Many of these altered transcripts have been described as crucial for oligodendrocyte lineage development and function, such as *Ptprz1*, *Gsn* (Brown and Verden, 2017), and *Map2* (Müller et al., 1997). Importantly, we discovered that the transcript encoding NF, a critical cell adhesion protein involved in node of Ranvier establishment and maintenance, was differentially spliced under the regulation of m^{6}A. The mouse *Nfasc* gene contains 39 exons, and the inclusion or exclusion of different *Nfasc* exons results in transcripts that encode functionally distinct isoforms (Suzuki et al., 2017). NF186 is expressed by neurons and is critical for node assembly, and NF155, which is expressed by the myelinating cells, is critical to the stability of the paranodal domain (Howell et al., 2006; Kawamura et al., 2013; Kira et al., 2019; Pomicter et al., 2010). The disruption of NF isoform distribution results in pathological changes in myelinated axons (Howell et al., 2006; Pillai et al., 2009; Thaxton et al., 2010). We identified aberrantly spliced *Nfasc* RNA isoforms in the *Mettl14*-deleted oligodendrocytes and provided *in vivo* evidence of altered NF155 protein expression that correlated with morphological abnormalities of the paranodal domain. In particular, the nodes of Ranvier in the CNS of adult *Mettl14$^{fl/fl}$;Olig2*-Cre mutants displayed widespread abnormalities, strikingly reminiscent of NF155-deficient mice (Pillai et al., 2009). These results indicate that m^{6}A RNA methylation regulates *Nfasc155* splicing and plays a role in establishing and maintaining normal function of critical axonal-oligodendrocyte interactions. Interestingly, changes in NF155 expression have recently been suggested to be central to adult myelin remodeling associated with altered impulse transmission (Fields and Dutta, 2019). This raises an intriguing possibility that the m^{6}A epigenetic mark plays a critical role in activity-dependent myelin remodeling.

A recent study reported that the proline-rich coiled-coil 2A (Prrc2a) protein is an m^{6}A reader that participates in oligodendrocyte specification and myelination by regulating the stability of its critical downstream target *Olig2* (Wu et al., 2019). Nevertheless, the clinical and pathological phenotypes of the oligodendrocyte-specific mouse mutants of *Prrc2a* are considerably more severe than that observed for the *Mett14* writer mutants described here, and the alteration in *Olig2* expression is also much more significant in the *Prrc2a* mutants. This raises the possibility that Prrc2a participates in other functions in addition to its putative role as an m^{6}A reader in oligodendrocyte lineage cells.

In conclusion, our study demonstrates that m^{6}A RNA modification is essential for normal oligodendrocyte maturation and CNS myelination. We show that the m^{6}A mark plays an important

Figure 8. *Mettl14* Deletion Results in Aberrant Node and Paranode Morphology

(A and B) Representative immunostaining with Caspr, Nfasc, and NaCh in P30 *Mettl14$^{fl/fl}$;Olig2*-Cre control (A) and mutant (B) corpus callosum. Representative nodes of Ranvier are shown in magnified windows (scale bars, 10 μm, 2 μm).

(C and D) Representative immunostaining with Caspr, Nfasc, and NaCh in P180 *Mettl14$^{fl/fl}$;Olig2*-Cre control (C) and mutant (D) corpus callosum. Representative nodes of Ranvier are shown in magnified windows (scale bars, 10 μm, 2 μm).

(E and G) Quantification of node number (NaCh positive) in P30 (E) and P180 (G) *Mettl14$^{fl/fl}$;Olig2*-Cre control and mutant corpus callosum. Node number count in mutants is normalized to controls (n = 3; *p < 0.05; **p < 0.01, unpaired Student's t test).

(F and H) Quantification of node (Caspr, NaCh positive) and paranode (Nfasc, Caspr double positive) size in P30 (F) and P180 (H) *Mettl14$^{fl/fl}$;Olig2*-Cre control and mutant corpus callosum. Node size in mutants is normalized to controls (control n = 2; mutant n = 3; *p < 0.05; **p < 0.01, unpaired Student's t test).

role in regulating various aspects of gene expression in oligodendrocyte lineage cells, with the most profound effects on mRNA levels and splicing. Rapid alterations to the m^{6}A landscape have the potential to quickly modify a cell's phenotypic properties (Geula et al., 2015; Licht and Jantsch, 2016; Yoon et al., 2017). Therefore, in addition to its critical role during development, the m^{6}A mark may participate in oligodendrocyte plasticity in adults. Future characterization of m^{6}A RNA epigenetic regulation should provide important insight to our growing understanding of the myelination process and demyelinating diseases.

STAR★METHODS

Detailed methods are provided in the online version of this paper and include the following:

- KEY RESOURCES TABLE
- LEAD CONTACT AND MATERIALS AVAILABILITY
  - Materials Availability Statement
- EXPERIMENTAL MODEL AND SUBJECT DETAILS
  - Animals
- METHOD DETAILS
  - OPC isolation and culture
  - OPC electroporation
  - Immunohistochemistry and cell counts
  - Immunocytochemistry
  - RNA scope
  - Electron Microscopy (EM) and analysis
  - Total protein isolation
  - Western blot
  - RNA isolation
  - RNA-seq and analysis
  - m^{6}A-SMART-seq and analysis
  - Differential alternative splicing analysis
- QUANTIFICATION AND STATISTICAL ANALYSIS
- DATA AND CODE AVAILABILITY

SUPPLEMENTAL INFORMATION

Supplemental Information can be found online at https://doi.org/10.1016/j.neuron.2019.12.013.

ACKNOWLEDGMENTS

This work was supported by the National Institutes of Health (NIH), United States (R01NS109372 to B.P., R35NS097370 to G.-l.M.), the National Multiple Sclerosis Society, United States (PP-1603-08106 to B.P.), and the Dr. Miriam and Sheldon G. Adelson Medical Research Foundation, United States to B.P. and G.-l.M. We thank the Genomics facility at the University of Chicago and the Bioinformatics core at the University of Illinois of Chicago for assistance. The Bioinformatics analysis in the project described was performed by the UIC Research Informatics Core, supported in part by National Center for Advancing Translational Sciences (NCATS), United States, through grant UL1TR002003. We also thank Dr. Ben Emery for generously providing MYRF antibody for this project and Dr. Vytas Bindokas, Dr. Xiaochang Zhang, Erdong Liu, Gloria Wright, and Ani Solanki for critical advice and assistance.

AUTHOR CONTRIBUTIONS

H.X. led the project, wrote the manuscript, and was involved in all aspects of the study. Y.D. contributed to RNA scope data and neurofascin immunohistochemistry. A.S. performed mRNA alternative splicing analysis. Y.-l.W. performed m^{6}A-seq and contributed to bioinformatics analysis. R.B.K. and Q.F. contributed to data collection and analysis. B.E. contributed to project design and interpretation of the experimental data. J.S.J. contributed to the bioinformatics analysis of m^{6}A-seq and RNA-seq data. Y.I.L. contributed to the critical discussion about alternative splicing analysis. X.Z. and C.H. contributed *Mettl14*$^{fl/fl}$ mice and critical discussion. G.-l.M. contributed to the m^{6}A-seq experiments and project design. B.P. conceived and designed the project. All authors contributed to the preparation of the manuscript.

DECLARATION OF INTERESTS

The authors declare no competing interests.

Received: December 10, 2018
Revised: October 15, 2019
Accepted: December 9, 2019
Published: December 31, 2019

REFERENCES

Aaker, J.D., Elbaz, B., Wu, Y., Looney, T.J., Zhang, L., Lahn, B.T., and Popko, B. (2016). Transcriptional fingerprint of hypomyelination in zfp191null and shiverer (mbpshi) mice. ASN Neuro *8*, 8.

Alarcón, C.R., Goodarzi, H., Lee, H., Liu, X., Tavazoie, S., and Tavazoie, S.F. (2015). HNRNPA2B1 Is a Mediator of m(6)A-Dependent Nuclear RNA Processing Events. Cell *162*, 1299–1308.

Batista, P.J., Molinie, B., Wang, J., Qu, K., Zhang, J., Li, L., Bouley, D.M., Lujan, E., Haddad, B., Daneshvar, K., et al. (2014). m(6)A RNA modification controls cell fate transition in mammalian embryonic stem cells. Cell Stem Cell *15*, 707–719.

Benjamini, Y., and Yekutieli, D. (2005). False discovery rate–adjusted multiple confidence intervals for selected parameters. J. Am. Stat. Assoc. *100*, 71–81.

Bergles, D.E., and Richardson, W.D. (2015). Oligodendrocyte development and plasticity. Cold Spring Harb. Perspect. Biol. *8*, a020453.

Bolger, A.M., Lohse, M., and Usadel, B. (2014). Trimmomatic: a flexible trimmer for Illumina sequence data. Bioinformatics, 2114–2120.

Bray, N.L., Pimentel, H., Melsted, P., and Pachter, L. (2016). Near-optimal probabilistic RNA-seq quantification. Nat. Biotechnol. *34*, 525–527.

Brockschnieder, D., Lappe-Siefke, C., Goebbels, S., Boesl, M.R., Nave, K.-A., and Riethmacher, D. (2004). Cell depletion due to diphtheria toxin fragment A after Cre-mediated recombination. Mol. Cell. Biol. *24*, 7636–7642.

Brown, T.L., and Verden, D.R. (2017). Cytoskeletal regulation of oligodendrocyte differentiation and myelination. J. Neurosci. *37*, 7797–7799.

Bujalka, H., Koenning, M., Jackson, S., Perreau, V.M., Pope, B., Hay, C.M., Mitew, S., Hill, A.F., Lu, Q.R., Wegner, M., et al. (2013). MYRF is a membrane-associated transcription factor that autoproteolytically cleaves to directly activate myelin genes. PLoS Biol. *11*, e1001625.

Carson, J.H., Worboys, K., Ainger, K., and Barbarese, E. (1997). Translocation of myelin basic protein mRNA in oligodendrocytes requires microtubules and kinesin. Cell Motil. Cytoskeleton *38*, 318–328.

Colman, D.R., Kreibich, G., Frey, A.B., and Sabatini, D.D. (1982). Synthesis and incorporation of myelin polypeptides into CNS myelin. J. Cell Biol. *95*, 598–608.

Coots, R.A., Liu, X.-M., Mao, Y., Dong, L., Zhou, J., Wan, J., Zhang, X., and Qian, S.-B. (2017). m^{6}A Facilitates eIF4F-Independent mRNA Translation. Mol. Cell *68*, 504–514.e7.

Copray, S., Huynh, J.L., Sher, F., Casaccia-Bonnefil, P., and Boddeke, E. (2009). Epigenetic mechanisms facilitating oligodendrocyte development, maturation, and aging. Glia *57*, 1579–1587.

Dobin, A., Davis, C.A., Schlesinger, F., Drenkow, J., Zaleski, C., Jha, S., Batut, P., Chaisson, M., and Gingeras, T.R. (2013). STAR: ultrafast universal RNA-seq aligner. Bioinformatics *29*, 15–21.

Elbaz, B., and Popko, B. (2019). Molecular control of oligodendrocyte development. Trends Neurosci. *42*, 263–277.

Emery, B., and Dugas, J.C. (2013). Purification of oligodendrocyte lineage cells from mouse cortices by immunopanning. Cold Spring Harb. Protoc. *2013*, 854–868.

Fields, R.D., and Dutta, D.J. (2019). Treadmilling model for plasticity of the myelin sheath. Trends Neurosci. *42*, 443–447.

Frye, M., Harada, B.T., Behm, M., and He, C. (2018). RNA modifications modulate gene expression during development. Science *361*, 1346–1349.

Fu, Y., Dominissini, D., Rechavi, G., and He, C. (2014). Gene expression regulation mediated through reversible m^6A RNA methylation. Nat. Rev. Genet. *15*, 293–306.

Geula, S., Moshitch-Moshkovitz, S., Dominissini, D., Mansour, A.A., Kol, N., Salmon-Divon, M., Hershkovitz, V., Peer, E., Mor, N., Manor, Y.S., et al. (2015). Stem cells. m6A mRNA methylation facilitates resolution of naïve pluripotency toward differentiation. Science *347*, 1002–1006.

Han, S.P., Friend, L.R., Carson, J.H., Korza, G., Barbarese, E., Maggipinto, M., Hatfield, J.T., Rothnagel, J.A., and Smith, R. (2010). Differential subcellular distributions and trafficking functions of hnRNP A2/B1 spliceoforms. Traffic *11*, 886–898.

Harroch, S., Furtado, G.C., Brueck, W., Rosenbluth, J., Lafaille, J., Chao, M., Buxbaum, J.D., and Schlessinger, J. (2002). A critical role for the protein tyrosine phosphatase receptor type Z in functional recovery from demyelinating lesions. Nat. Genet. *32*, 411–414.

Haussmann, I.U., Bodi, Z., Sanchez-Moran, E., Mongan, N.P., Archer, N., Fray, R.G., and Soller, M. (2016). m^6A potentiates Sxl alternative pre-mRNA splicing for robust Drosophila sex determination. Nature *540*, 301–304.

Hernandez, M., and Casaccia, P. (2015). Interplay between transcriptional control and chromatin regulation in the oligodendrocyte lineage. Glia *63*, 1357–1375.

Hoek, K.S., Kidd, G.J., Carson, J.H., and Smith, R. (1998). hnRNP A2 selectively binds the cytoplasmic transport sequence of myelin basic protein mRNA. Biochemistry *37*, 7021–7029.

Howell, O.W., Palser, A., Polito, A., Melrose, S., Zonta, B., Scheiermann, C., Vora, A.J., Brophy, P.J., and Reynolds, R. (2006). Disruption of neurofascin localization reveals early changes preceding demyelination and remyelination in multiple sclerosis. Brain *129*, 3173–3185.

Huber, W., Carey, V.J., Gentleman, R., Anders, S., Carlson, M., Carvalho, B.S., Bravo, H.C., Davis, S., Gatto, L., Girke, T., et al. (2015). Orchestrating high-throughput genomic analysis with Bioconductor. Nat. Methods *12*, 115–121.

Ivanova, I., Much, C., Di Giacomo, M., Azzi, C., Morgan, M., Moreira, P.N., Monahan, J., Carrieri, C., Enright, A.J., and O'Carroll, D. (2017). The RNA m^6A Reader YTHDF2 Is Essential for the Post-transcriptional Regulation of the Maternal Transcriptome and Oocyte Competence. Mol. Cell *67*, 1059–1067.e4.

Kawamura, N., Yamasaki, R., Yonekawa, T., Matsushita, T., Kusunoki, S., Nagayama, S., Fukuda, Y., Ogata, H., Matsuse, D., Murai, H., and Kira, J. (2013). Anti-neurofascin antibody in patients with combined central and peripheral demyelination. Neurology *81*, 714–722.

Kira, J.-I., Yamasaki, R., and Ogata, H. (2019). Anti-neurofascin autoantibody and demyelination. Neurochem. Int. *130*, 104360.

Koranda, J.L., Dore, L., Shi, H., Patel, M.J., Vaasjo, L.O., Rao, M.N., Chen, K., Lu, Z., Yi, Y., Chi, W., et al. (2018). Mettl14 is essential for epitranscriptomic regulation of striatal function and learning. Neuron *99*, 283–292.e5.

Koreman, E., Sun, X., and Lu, Q.R. (2018). Chromatin remodeling and epigenetic regulation of oligodendrocyte myelination and myelin repair. Mol. Cell. Neurosci. *87*, 18–26.

Lappe-Siefke, C., Goebbels, S., Gravel, M., Nicksch, E., Lee, J., Braun, P.E., Griffiths, I.R., and Nave, K.-A. (2003). Disruption of Cnp1 uncouples oligodendroglial functions in axonal support and myelination. Nat. Genet. *33*, 366–374.

Li, H., and Richardson, W.D. (2009). Genetics meets epigenetics: HDACs and Wnt signaling in myelin development and regeneration. Nat. Neurosci. *12*, 815–817.

Li, Z., Weng, H., Su, R., Weng, X., Zuo, Z., Li, C., Huang, H., Nachtergaele, S., Dong, L., Hu, C., et al. (2017). FTO Plays an Oncogenic Role in Acute Myeloid Leukemia as a N^6-Methyladenosine RNA Demethylase. Cancer Cell *31*, 127–141.

Li, Y.I., Knowles, D.A., Humphrey, J., Barbeira, A.N., Dickinson, S.P., Im, H.K., and Pritchard, J.K. (2018). Annotation-free quantification of RNA splicing using LeafCutter. Nat. Genet. *50*, 151–158.

Licht, K., and Jantsch, M.F. (2016). Rapid and dynamic transcriptome regulation by RNA editing and RNA modifications. J. Cell Biol. *213*, 15–22.

Liu, J., Yue, Y., Han, D., Wang, X., Fu, Y., Zhang, L., Jia, G., Yu, M., Lu, Z., Deng, X., et al. (2014). A METTL3-METTL14 complex mediates mammalian nuclear RNA N6-adenosine methylation. Nat. Chem. Biol. *10*, 93–95.

Liu, J., Moyon, S., Hernandez, M., and Casaccia, P. (2016). Epigenetic control of oligodendrocyte development: adding new players to old keepers. Curr. Opin. Neurobiol. *39*, 133–138.

Marin-Husstege, M., Muggironi, M., Liu, A., and Casaccia-Bonnefil, P. (2002). Histone deacetylase activity is necessary for oligodendrocyte lineage progression. J. Neurosci. *22*, 10333–10345.

Mitew, S., Hay, C.M., Peckham, H., Xiao, J., Koenning, M., and Emery, B. (2014). Mechanisms regulating the development of oligodendrocytes and central nervous system myelin. Neuroscience *276*, 29–47.

Montague, P., McCallion, A.S., Davies, R.W., and Griffiths, I.R. (2006). Myelin-associated oligodendrocytic basic protein: a family of abundant CNS myelin proteins in search of a function. Dev. Neurosci. *28*, 479–487.

Moyon, S., and Casaccia, P. (2017). DNA methylation in oligodendroglial cells during developmental myelination and in disease. Neurogenesis (Austin) *4*, e1270381.

Müller, R., Heinrich, M., Heck, S., Blohm, D., and Richter-Landsberg, C. (1997). Expression of microtubule-associated proteins MAP2 and tau in cultured rat brain oligodendrocytes. Cell Tissue Res. *288*, 239–249.

Müller, C., Bauer, N.M., Schäfer, I., and White, R. (2013). Making myelin basic protein -from mRNA transport to localized translation. Front. Cell. Neurosci. *7*, 169.

Nave, K.-A., and Werner, H.B. (2014). Myelination of the nervous system: mechanisms and functions. Annu. Rev. Cell Dev. Biol. *30*, 503–533.

Nishiyama, A., Komitova, M., Suzuki, R., and Zhu, X. (2009). Polydendrocytes (NG2 cells): multifunctional cells with lineage plasticity. Nat. Rev. Neurosci. *10*, 9–22.

Picelli, S., Faridani, O.R., Björklund, A.K., Winberg, G., Sagasser, S., and Sandberg, R. (2014). Full-length RNA-seq from single cells using Smart-seq2. Nat. Protoc. *9*, 171–181.

Pillai, A.M., Thaxton, C., Pribisko, A.L., Cheng, J.-G., Dupree, J.L., and Bhat, M.A. (2009). Spatiotemporal ablation of myelinating glia-specific neurofascin (Nfasc NF155) in mice reveals gradual loss of paranodal axoglial junctions and concomitant disorganization of axonal domains. J. Neurosci. Res. *87*, 1773–1793.

Pomicter, A.D., Shroff, S.M., Fuss, B., Sato-Bigbee, C., Brophy, P.J., Rasband, M.N., Bhat, M.A., and Dupree, J.L. (2010). Novel forms of neurofascin 155 in the central nervous system: alterations in paranodal disruption models and multiple sclerosis. Brain *133*, 389–405.

Ravanelli, A.M., and Appel, B. (2015). Motor neurons and oligodendrocytes arise from distinct cell lineages by progenitor recruitment. Genes Dev. *29*, 2504–2515.

Roundtree, I.A., Luo, G.-Z., Zhang, Z., Wang, X., Zhou, T., Cui, Y., Sha, J., Huang, X., Guerrero, L., Xie, P., et al. (2017). YTHDC1 mediates nuclear export of N^6-methyladenosine methylated mRNAs. eLife *6*, 6.

Rowitch, D.H. (2004). Glial specification in the vertebrate neural tube. Nat. Rev. Neurosci. *5*, 409–419.

Schüller, U., Heine, V.M., Mao, J., Kho, A.T., Dillon, A.K., Han, Y.-G., Huillard, E., Sun, T., Ligon, A.H., Qian, Y., et al. (2008). Acquisition of granule neuron precursor identity is a critical determinant of progenitor cell competence to form Shh-induced medulloblastoma. Cancer Cell *14*, 123–134.

Sherman, D.L., Tait, S., Melrose, S., Johnson, R., Zonta, B., Court, F.A., Macklin, W.B., Meek, S., Smith, A.J.H., Cottrell, D.F., and Brophy, P.J. (2005). Neurofascins are required to establish axonal domains for saltatory conduction. Neuron *48*, 737–742.

Shi, H., Wang, X., Lu, Z., Zhao, B.S., Ma, H., Hsu, P.J., Liu, C., and He, C. (2017). YTHDF3 facilitates translation and decay of N^6-methyladenosine-modified RNA. Cell Res. *27*, 315–328.

Simons, M., and Nave, K.-A. (2015). Oligodendrocytes: myelination and axonal support. Cold Spring Harb. Perspect. Biol. *8*, a020479.

Sommer, I., and Schachner, M. (1981). Monoclonal antibodies (O1 to O4) to oligodendrocyte cell surfaces: an immunocytological study in the central nervous system. Dev. Biol. *83*, 311–327.

Suzuki, S., Ayukawa, N., Okada, C., Tanaka, M., Takekoshi, S., Iijima, Y., and Iijima, T. (2017). Spatio-temporal and dynamic regulation of neurofascin alternative splicing in mouse cerebellar neurons. Sci. Rep. *7*, 11405.

Thakurela, S., Garding, A., Jung, R.B., Müller, C., Goebbels, S., White, R., Werner, H.B., and Tiwari, V.K. (2016). The transcriptome of mouse central nervous system myelin. Sci. Rep. *6*, 25828.

Thaxton, C., Pillai, A.M., Pribisko, A.L., Labasque, M., Dupree, J.L., Faivre-Sarrailh, C., and Bhat, M.A. (2010). In vivo deletion of immunoglobulin domains 5 and 6 in neurofascin (Nfasc) reveals domain-specific requirements in myelinated axons. J. Neurosci. *30*, 4868–4876.

Wang, X., Lu, Z., Gomez, A., Hon, G.C., Yue, Y., Han, D., Fu, Y., Parisien, M., Dai, Q., Jia, G., et al. (2014). N6-methyladenosine-dependent regulation of messenger RNA stability. Nature *505*, 117–120.

Wang, X., Zhao, B.S., Roundtree, I.A., Lu, Z., Han, D., Ma, H., Weng, X., Chen, K., Shi, H., and He, C. (2015). N(6)-methyladenosine Modulates Messenger RNA Translation Efficiency. Cell *161*, 1388–1399.

Wang, Y., Li, Y., Yue, M., Wang, J., Kumar, S., Wechsler-Reya, R.J., Zhang, Z., Ogawa, Y., Kellis, M., Duester, G., and Zhao, J.C. (2018). N^6-methyladenosine RNA modification regulates embryonic neural stem cell self-renewal through histone modifications. Nat. Neurosci. *21*, 195–206.

Weng, H., Huang, H., Wu, H., Qin, X., Zhao, B.S., Dong, L., Shi, H., Skibbe, J., Shen, C., Hu, C., et al. (2018a). METTL14 Inhibits Hematopoietic Stem/Progenitor Differentiation and Promotes Leukemogenesis via mRNA m^6A Modification. Cell Stem Cell *22*, 191–205.e9.

Weng, Y.-L., Wang, X., An, R., Cassin, J., Vissers, C., Liu, Y., Liu, Y., Xu, T., Wang, X., Wong, S.Z.H., et al. (2018b). Epitranscriptomic m6a regulation of axon regeneration in the adult mammalian nervous system. Neuron *97*, 313–325.e6.

Wu, R., Li, A., Sun, B., Sun, J.-G., Zhang, J., Zhang, T., Chen, Y., Xiao, Y., Gao, Y., Zhang, Q., et al. (2019). A novel m^6A reader Prrc2a controls oligodendroglial specification and myelination. Cell Res. *29*, 23–41.

Xiao, W., Adhikari, S., Dahal, U., Chen, Y.-S., Hao, Y.-J., Sun, B.-F., Sun, H.-Y., Li, A., Ping, X.-L., Lai, W.-Y., et al. (2016). Nuclear m(6)A Reader YTHDC1 Regulates mRNA Splicing. Mol. Cell *61*, 507–519.

Xu, K., Yang, Y., Feng, G.-H., Sun, B.-F., Chen, J.-Q., Li, Y.-F., Chen, Y.-S., Zhang, X.-X., Wang, C.-X., Jiang, L.-Y., et al. (2017). Mettl3-mediated m^6A regulates spermatogonial differentiation and meiosis initiation. Cell Res. *27*, 1100–1114.

Ye, F., Chen, Y., Hoang, T., Montgomery, R.L., Zhao, X.H., Bu, H., Hu, T., Taketo, M.M., van Es, J.H., Clevers, H., et al. (2009). HDAC1 and HDAC2 regulate oligodendrocyte differentiation by disrupting the beta-catenin-TCF interaction. Nat. Neurosci. *12*, 829–838.

Yoon, K.-J., Ringeling, F.R., Vissers, C., Jacob, F., Pokrass, M., Jimenez-Cyrus, D., Su, Y., Kim, N.-S., Zhu, Y., Zheng, L., et al. (2017). Temporal control of mammalian cortical neurogenesis by m6a methylation. Cell *171*, 877–889.e17.

Yue, Y., Liu, J., and He, C. (2015). RNA N6-methyladenosine methylation in post-transcriptional gene expression regulation. Genes Dev. *29*, 1343–1355.

Zhang, Y., Chen, K., Sloan, S.A., Bennett, M.L., Scholze, A.R., O'Keeffe, S., Phatnani, H.P., Guarnieri, P., Caneda, C., Ruderisch, N., et al. (2014). An RNA-sequencing transcriptome and splicing database of glia, neurons, and vascular cells of the cerebral cortex. J. Neurosci. *34*, 11929–11947.

Zhang, C., Chen, Y., Sun, B., Wang, L., Yang, Y., Ma, D., Lv, J., Heng, J., Ding, Y., Xue, Y., et al. (2017). m^6A modulates haematopoietic stem and progenitor cell specification. Nature *549*, 273–276.

Zhao, B.S., and He, C. (2017). "Gamete On" for m^6A: YTHDF2 Exerts Essential Functions in Female Fertility. Mol. Cell *67*, 903–905.

Zhao, L., Mandler, M.D., Yi, H., and Feng, Y. (2010a). Quaking I controls a unique cytoplasmic pathway that regulates alternative splicing of myelin-associated glycoprotein. Proc. Natl. Acad. Sci. USA *107*, 19061–19066.

Zhao, X., He, X., Han, X., Yu, Y., Ye, F., Chen, Y., Hoang, T., Xu, X., Mi, Q.-S., Xin, M., et al. (2010b). MicroRNA-mediated control of oligodendrocyte differentiation. Neuron *65*, 612–626.

Zhao, X., Yang, Y., Sun, B.-F., Shi, Y., Yang, X., Xiao, W., Hao, Y.-J., Ping, X.-L., Chen, Y.-S., Wang, W.-J., et al. (2014). FTO-dependent demethylation of N6-methyladenosine regulates mRNA splicing and is required for adipogenesis. Cell Res. *24*, 1403–1419.

Zhou, Q., and Anderson, D.J. (2002). The bHLH transcription factors OLIG2 and OLIG1 couple neuronal and glial subtype specification. Cell *109*, 61–73.

Zhou, J., Wan, J., Shu, X.E., Mao, Y., Liu, X.-M., Yuan, X., Zhang, X., Hess, M.E., Brüning, J.C., and Qian, S.-B. (2018). N^6-Methyladenosine Guides mRNA Alternative Translation during Integrated Stress Response. Mol. Cell *69*, 636–647.e7.

Zhou, K.I., Shi, H., Lyu, R., Wylder, A.C., Matuszek, Ż., Pan, J.N., He, C., Parisien, M., and Pan, T. (2019). Regulation of Co-transcriptional Pre-mRNA Splicing by m^6A through the Low-Complexity Protein hnRNPG. Mol. Cell *76*, 70–81.e9.

Zonta, B., Tait, S., Melrose, S., Anderson, H., Harroch, S., Higginson, J., Sherman, D.L., and Brophy, P.J. (2008). Glial and neuronal isoforms of Neurofascin have distinct roles in the assembly of nodes of Ranvier in the central nervous system. J. Cell Biol. *181*, 1169–1177.

Zuchero, J.B., and Barres, B.A. (2013). Intrinsic and extrinsic control of oligodendrocyte development. Curr. Opin. Neurobiol. *23*, 914–920.

Zuchero, J.B., and Barres, B.A. (2015). Glia in mammalian development and disease. Development *142*, 3805–3809.

STAR★METHODS

KEY RESOURCES TABLE

REAGENT or RESOURCE	SOURCE	IDENTIFIER
Antibodies		
Rabbit anti-METTL14	Sigma-Aldrich	Cat# HPA038002; RRID: AB_10672401
Goat anti-PDGFR-α	R&D Systems	Cat# AF1062; RRID: AB_2236897
Rabbit anti-MBP	Abcam	Cat# ab40390; RRID: AB_1141521
Mouse anti-CC1	Millipore	Cat# OP80; RRID: AB_2057371
Mouse anti-Olig2	Millipore	Cat# MABN50; RRID: AB_10807410
Mouse anti-O1	R&D Systems	Cat# MAB1327; RRID: AB_357618
Rabbit anti-Ki67	Abcam	Cat# AB15580; RRID: AB_805388
Rabbit anti-MAG	Thermo Fisher Scientific	Cat# 34-6200, RRID: AB_2533179
Mouse anti-MBP	BioLegend	Cat# SMI 99; RRID: AB_2314771
Mouse anti-MYRF	Generous gift from Dr. Ben Emery	Cat# 4G4; RRID: AB_2814997
Mouse anti-GAPDH	Cell Signaling	Cat# 2118; RRID: AB_561053
Chicken anti-Neurofascin, pan	R&D Systems	Cat# AF3235; RRID: AB_10890736
Rabbit anti-Caspr	Abcam	Cat# ab34151; RRID: AB_869934
Mouse anti-Sodium channel, pan	Sigma-Aldrich	Cat# S8809; RRID: AB_477552
Rabbit anti-Choline acetyltransferase (ChAT)	Millipore	Cat# AB144P; RRID: AB_2079751
Goat anti-mouse IgG+IgM	Jackson ImmunoResearch	Cat# 115-055-044; RRID: AB_2338532
Goat anti-mouse IgM	Jackson ImmunoResearch	Cat# 115-005-020; RRID: AB_2338450
Mouse IgG HRP Linked Whole Antibody	GE Healthcare	Cat# NA931; RRID: AB_772210
Rabbit IgG HRP-Linked Whole Antibody	GE Healthcare	Cat# NA934; RRID: AB_772206
Rabbit anti-Chicken IgY (H+L) Secondary Antibody, HRP	Thermo Fisher Scientific	Cat# 31401; RRID: AB_228385
Donkey Anti-mouse IgG (H+L), Alexa Fluor 488	Thermo Fisher Scientific	Cat# A-21202; RRID: AB_141607
Donkey Anti-Rabbit IgG (H+L) Antibody, Alexa Fluor 488	Thermo Fisher Scientific	Cat# A-21206; RRID: AB_2535792
Donkey Anti-Mouse IgG (H+L), Alexa Fluor 594	Thermo Fisher Scientific	Cat# A-21203; RRID: AB_2535789
Donkey Anti-Goat IgG (H+L), Alexa Fluor 594	Thermo Fisher Scientific	Cat# A-11058; RRID: AB_2534105
Donkey Anti-Rabbit IgG (H+L), Alexa Fluor 594	Thermo Fisher Scientific	Cat# A-21207; RRID: AB_141637
Goat anti-Chicken IgY (H+L) Secondary Antibody, Alexa Fluor 594	Thermo Fisher Scientific	Cat# A-11042; RRID: AB_2534099
Chemicals, Peptides, and Recombinant Proteins		
RNAscope Probe –Mm-Myrf	ACD bio	Cat# 524061
RNAscope Probe –Mm-Mbp	ACD bio	Cat# 451491
Dynabeads Oligo$(dT)_{25}$	Thermo Fisher Scientific	Cat# 61006
Dynabeads Protein A	Thermo Fisher Scientific	Cat# 1001D
N^6-Methyladenosine 5′-monophosphate sodium salt	Sigma-Aldrich	Cat# M2780
Poly-D-lysine	Sigma-Aldrich	Cat# P6407
Platelet derived growth factor	PeproTech	Cat# 100-13A
Neurotrophin-3	PeproTech	Cat# 450-03
Ciliary neurotrophic factor	PeproTech	Cat# 450-13

(*Continued on next page*)

Continued

REAGENT or RESOURCE	SOURCE	IDENTIFIER
Forskolin	Sigma-Aldrich	Cat# F6886
B27	Life technologies	Cat# 17504044
Fetal bovine serum	Atlanta Biologicals	Cat# S11050
Normal donkey serum	Jackson ImmunoResearch	Cat# 017-000-121
Protease inhibitor cocktail	Thermo Fisher Scientific	Cat# 78430
Phosphatase inhibitors	Sigma-Aldrich	Cat# P2850 and P5726
Laemmli sample buffer	Bio-Rad Laboratories	Cat# 161-0737
β-mercaptoethanol	Sigma-Aldrich	Cat# M6250
Trizol reagent	Thermo Fisher Scientific	Cat# 15596018
Triiodothyronine	Sigma-Aldrich	Cat# T6397
Trypsin 0.05%	Thermo Fisher Scientific	Cat# 25300-054
Trypsin 2.5%	Thermo Fisher Scientific	Cat# 15090046
Trypsin inhibitor	Worthington	Cat# LS003086
Deoxyribonuclease I	Worthington	Cat# LS002007
Papain	Worthington	Cat# LS003126
Apo transferrin	Sigma-Aldrich	Cat# T1147
ProLong gold abtifade reagent with DAPI	Life Technologies	Cat# P36931
Paraformadehyde	Thermo Fisher Scientific	Cat# T353-500
Osmium Tetroxide	Electron Microscopy Science	Cat# 19152
Propylene Oxide	Electron Microscopy Science	Cat# 20401
Sodium Cacodylate Buffer	Electron Microscopy Science	Cat# 11652
Epon 812	Electron Microscopy Science	Cat# 14900
Critical Commercial Assays		
BCA Protein Assay Kit	Thermo Fisher Scientific	Cat# 23255
Aurum Total RNA mini Kit	Bio-Rad Laboratories	Cat# 732-6820
Agilent RNA 6000 Nano kit with chips	Agilent	Cat# 5067-1511
RNA Clean & Concentrator	Zymo	Cat# R1015
NEBNext Ultra RNA library Prep kit for Illumina	New England Biolabs	Cat# 61011
RNA Fragmentation Reagents	Thermo Fisher Scientific	Cat# AM8740
Dynabeads Oligo$(dT)_{25}$	Thermo Fisher Scientific	Cat# 61006
SuperSignal West Dura Extended Duration Substrate	Thermo Fisher Scientific	Cat# 34076
Pierce™ ECL Western Blotting Substrate	Thermo Fisher Scientific	Cat# 32209
SMARTScribe Reverse Transcriptase	Clontech	Cat# 639537
Protein A Dynabeads	Thermo Fisher Scientific	Cat# 0002D
Advantage 2 Polymerase Mix	Thermo Fisher Scientific	Cat# 639201
Agencourt AMPure XP	Beckman Coulter	Cat# A63880
RNAScope Multiplex Fluorescent V2 Assay kit	ACD bio	Cat# 323110
Basic NucleofectorTM Kit for Primary Mammalian Glial Cells	Lonza	Cat# VPI-1006
Opal™ 520	Akoya Biosciences	Cat# FP1487001KT
Opal™ 620	Akoya Biosciences	Cat# FP1495001KT
Deposited Data		
Raw and analyzed data	This paper	GEO: GSE124244

(*Continued on next page*)

Continued		
REAGENT or RESOURCE	SOURCE	IDENTIFIER
Experimental Models: Organisms/Strains		
Mouse: *Mettl14*$^{fl/fl}$	Generous gift from Dr. Xiaoxi Zhuang	Koranda et al., 2018; Weng et al., 2018b; Yoon et al., 2017
Mouse: *Olig2*-Cre	Generous gift from Dr. David Rowitch	The Jackson Laboratory: 011103
Mouse: *CNP*-Cre	Generous gift from Dr. Klaus Amin Nave	MGI: 3051635
Oligonucleotides		
RT-PCR primers for *Nfasc* aberrant spliced locus: Forward: ACTGGGAAAGCAGATGGTGG Reverse: ACATGAGCCCGATGAACCAG	This paper	Figure 7
Recombinant DNA		
Mettl14 (NM_201638) Mouse Tagged ORF Clone	OriGene	Cat# MR207291
pmaxGFP™ vector	Lonza	Cat# VPI-1006
Software and Algorithms		
ImageJ	National Institutes of Health	RRID: SCR_003070
Image Lab	Bio-Rad Laboratories	RRID: SCR_014210
R v3.5.1	R core team	RRID: SCR_001905
Bioconductor v.3.7	Huber et al., 2015	RRID: SCR_006442
STAR v2.6.1a	Dobin et al., 2013	RRID: SCR_015899
Trimmomatic	Bolger et al., 2014	RRID: SCR_011848
Kallisto v0.44.0	Bray et al., 2016	RRID: SCR_016582
GraphPad Prism 6	GraphPad Software	RRID: SCR_002798
LeafCutter	Li et al.,2018	RRID: SCR_017639

LEAD CONTACT AND MATERIALS AVAILABILITY

Further information and requests for resources and reagents should be directed to and will be fulfilled by the Lead Contact Brian Popko (brian.popko@northwestern.edu).

Materials Availability Statement

This study did not generate new unique reagents.

EXPERIMENTAL MODEL AND SUBJECT DETAILS

Animals

All animals were housed under pathogen-free conditions, and all animal procedures and animal care were conducted in accordance with guidelines approved by the University of Chicago's Institutional Animal Care and Use Community (IACUC). All mice were on the C57BL/6 background, and both female and male mice were used.

Mettl14$^{fl/fl}$ mice (Koranda et al., 2018; Weng et al., 2018b; Yoon et al., 2017) were crossed with *Olig2*-Cre mice (Schüller et al., 2008), and *CNP*-Cre mice (Lappe-Siefke et al., 2003). *Mettl14*$^{fl/fl}$*;Olig2*-Cre and littermate control *Mettl14*$^{fl/fl}$ mice as well as *Mettl14*$^{fl/fl}$*;CNP*-Cre and littermate control *Mettl14*$^{fl/fl}$ mice were used for experiments.

METHOD DETAILS

OPC isolation and culture

OPCs were isolated and purified (95% purity) from postnatal day 6 (P6) mouse brains using an immunopanning protocol (Emery and Dugas, 2013). In brief, mice pups (both female and male) were genotyped and marked at P4-P5. At P6, pups were deeply anaesthetized on ice and cortices were collected, diced, and digested with papain at 37°C. Cells were then triturated into a single cell suspension, then sequentially immunopanned in Ran-2, GalC, and O4 antibodies from hybridomal supernatant. The remaining O4^{+}GalC^{-} cells (OPCs) were then trypsinized and plated in poly-d-Lysine (PDL)-coated plates with proliferation media. Once OPCs numbers reach sufficient amount, they were split and plated in differentiation media.

OPC electroporation

Amaxa cell nucleofector II device and an electroporation kit for primary mammalian glial cells (Lonza, Cat# VPI-1006) were used as per the manufacturer's instructions for OPC electroporation. For each biological replicate, 5 million OPCs were collected and transfected with both pmaxGFP Vector (Lonza, Cat# VPI-1006) and *Mettl14* plasmid (Origene, Cat# MR207291) or pmaxGFP Vector alone. Transfected OPCs were then plated in PDL coated plates with differentiation media. Transfection efficiency was about 40%, measured by GFP positive cell number versus total cell number after 72 h of electroporation.

Immunohistochemistry and cell counts

Mice were deeply anaesthetized with 2.5% avertin (Cat# T48402, Sigma Aldrich) in dH2O. Upon the loss of nociceptive reflexes, mice were transcardially perfused with 0.9% saline followed by ice-cold 4% paraformaldehyde (PFA). Brains were collected and post-fixed overnight in 4% PFA at 4°C, followed by incubation in 30% sucrose until saturation. Tissues were then embedded in optimal cutting temperature compound (OCT) and sectioned at 10μm. Prior to Rabbit-anti-METTL14 (1:300, Sigma, Cat# HPA038002), Goat-anti-PDGFR-α (1:100, R and D systems, Cat# AF1062), Rabbit-anti-Ki67 (1:100, Abcam, Cat# ab15580), Chicken-anti-Neurofascin (1:50, R and D systems, Cat# AF3235), Mouse-anti-sodium channel (1:100, Sigma, Cat# S8809) and Rabbit-anti-Caspr (1:300, Abcam, Cat# ab34151) immunostaining, tissue sections were processed with an antibody retrieval protocol in which sections were treated with 10 mM trisodium citrate buffer (pH 6.0) at 90°C for 30 min. After cooling at room temperature (RT) for 30 min, sections were then incubated in 10 mM glycine (in TBS with 0.25% Triton X-100) for 1 h at RT. Slices were then blocked with TBS containing 5% normal donkey serum, 1% BSA and 0.25% Triton X-100 (blocking buffer) for 2 h at RT, followed by incubation in primary antibody(s) diluted in blocking buffer for 48 h at 4°C. Immunohistochemistry with Rabbit-anti-MBP (1:500, Abcam, Cat# ab40390), Mouse-anti-CC1 (1:50, Milipore, Cat# OP80), Mouse-anti-Olig2 (1:100, Milipore, Cat# MABN50) and Rabbit-anti-ChAT (1:300, Milipore, Cat# AB144P) antibodies, were followed by immunostaining protocol without antigen retrieval.

Stained tissue sections were imaged with a Mariana Yokogawa-type spinning disk confocal microscope or Leica TCS SP5 two-photon confocal microscope. All experimental and littermate control tissues were imaged with the same parameters, followed with the same adjustments in ImageJ. Cells counts data were converted to cells/100 μm^2.

Immunocytochemistry

Cells cultured on coverslips were rinsed with PBS and fixed with ice cold 4% PFA for 10 min at RT, washed with PBS, then air-dried and stored at −80°C until immunostaining. The primary antibodies used were Rabbit-anti-MBP (1:500, Abcam, Cat# ab40390), Goat-anti-PDGFR-α (1:100, R and D systems, Cat# AF1062) and Mouse-anti-O1 (1:100, R and D systems, Cat# MAB1327). Immunocytochemistry was conducted using the normal immunostaining protocol as described above, without the antigen retrieval process.

RNA scope

Mouse *Myrf* mRNA probe (ACDbio, Cat# 524061), mouse *Mbp* mRNA probe (ACDbio, Cat# 451491) and RNAscope Multiplex Fluorescent Reagent Kit V2 assay (ACDbio, Cat# 323110) were purchased from ACDbio company. Fluorophores were purchased from Akoya biosciences (Opal 520: Cat# FP1487001KT, Opal 620: Cat# FP1495001KT). Mice were processed for RNAscope as follows. Deeply anesthetized animals were transcardially perfused with 0.9% saline followed by ice-cold 4% PFA as described above. Brains were immediately dissected out and transferred to 10% NB formalin solution (Sigma, Cat# HT5011) at RT for exactly 24 h. Brains were then transferred to freshly made 70% ethanol for 24 h at RT and processed for paraffin embedding. Sections were cut at 5 μm. RNAscope assay was performed as per manufacturer's specifications.

Electron Microscopy (EM) and analysis

Mice were deeply anesthetized with 2.5% avertin, followed by perfusion with 0.9% saline and 0.1M sodium cacodylate buffer containing 4% PFA and 2.5% glutaraldehyde (EM buffer). Corpus callosum and optic nerve were then post-fixed overnight at 4°C. Tissues were dissected and washed with 0.1M sodium cacodylate buffer for 3 times, followed by post fixation with 1% osmium tetroxide (diluted with 0.1M sodium cacodylate) for 2 h and another 3 times of wash with 0.1M sodium cacodylate buffer. These tissue samples then went through dehydration steps with 30%, 50%, 70%, 90%, 95%,100% ethanol and propylene oxide (PO), followed by permeation with 1:1 PO/Epon 812 and 1:2 PO/Epon 812 for 2 h each, and in Epon 812 overnight at RT. The next morning, samples were permeated with Epon 812 for another 4 h at RT, and then embedded with labeled paper strips in fresh Epon 812. These samples were then cured for 48 h in a 60°C oven. After EM processing steps, samples were sectioned (1μm) and stained with toluidine blue, before sectioned into ultrathin slices (60-90nm) and stained with uranyl acetate-lead citrate. FEI Tecnai F30 scanning transmission electron microscope (FEI company) was used to take EM images. ImageJ was used to analyze the EM images for g-ratio and axon counting.

Total protein isolation

Cells in culture were rinsed with sterile PBS 2 times, then lysed with ice-cold RIPA buffer containing protease inhibitors (Thermo Fisher Scientific, Cat# 78430) and phosphatase inhibitors (Sigma, Cat# P2850 and P5726)(lysis buffer), and then scraped and collected in microcentrifuge tubes for 10 min incubation on ice. Cell lysates were then centrifuged at 13,000 g for 15 min at 4°C, and supernatant was collected and stored in −80°C until measurement. To collect brain tissues, mice were deeply anesthetized with 2.5% avertin and perfused with ice-cold sterile PBS, followed by brain isolation into microcentrifuge tubes and immediately

frozen in liquid nitrogen. Brain samples were then stored in −80°C until homogenization. Brain tissue protein lysates were prepared as follows: homogenized in lysis buffer, incubated on ice for 15 min and centrifuged at 13,000 g for 15 min at 4°C, then collect supernatants. Protein concentration was determined by using a BCA Protein Assay Kit (Thermo Fisher Scientific, Cat# 23255) as per the manufacturer's instructions.

Western blot

Protein lysates were boiled for 5 min in Laemmli sample buffer (Bio-Rad, Cat# 161-0737) with β-mercaptoethanol (Sigma, Cat# M6250), seperated by SDS-PAGE, transferred to nitrocellulose membrane and immunoblotted. The primary antibodies used were Rabbit-anti-METTL14 (1:1000, Sigma, Cat# HPA038002); Rabbit-anti-MBP (1:1000, Abcam, Cat# ab40390), Rabbit-anti-MAG (1:1000, Thermo Fisher Scientific, Cat# AB_2533179), Mouse-anti-Olig2 (1:1000, Millipore, Cat# MABN50), Mouse-anti-MYRF (1:5000, gift from Dr. Ben Emery), GAPDH(1:2000, Cell signaling, Cat# 2118S). Western blot bands were analyzed in Image Lab software (Bio-Rad laboratories).

RNA isolation

Cell and tissue RNA samples were prepared and isolated following the manufacture's protocol (Bio-Rad, Cat# 732-6820). RNA quality was confirmed by 2100 Bioanalyzer using a model 6000 Nano kit (Agilent technologies, Cat# 5067-1511). Samples with RNA integrity number > 8 were used.

RNA-seq and analysis

Bulk RNA-seq was performed on RNA isolated from cultured OPCs and oligodendrocytes as previously described (Aaker et al., 2016). Libraries were prepared and sequenced using the Illumina HiSeq 4000 at the University of Chicago Genomics Core facility. Reads were mapped using both STAR v2.6.1a and Kallisto v.0.44.0 using bowtie 2 aligner (Bray et al., 2016; Dobin et al., 2013). Mapped reads were further analyzed with the Bioconductor suite v3.7 by the University of Illinois at Chicago Bioinformatics Core facility (Huber et al., 2015). Q-values were determined as false discovery rate adjusted p values using the method previously described (Benjamini and Yekutieli, 2005). Results were compared with the m^{6}A-SMART-Seq analysis and visualized in R v.3.5.1 using the plot.ly, ggplot2, and venn.diagram packages. Values for expression, fold change, and statistical significance were adapted for visualization using a $\log_2$ transformation.

m^{6}A-SMART-seq and analysis

mRNA from total RNA of OPCs and oligodendrocytes was purified with Dynabeads Oligo $(dT)_{25}$ (Thermo Fisher Scientific, Cat# 61006). The purified mRNA was then processed for m^{6}A-SMART-seq and analyzed as previously described (Weng et al., 2018b). Z scores were calculated for each m^{6}A mark and filtered with a threshold value of 0.

Differential alternative splicing analysis

Differential splicing analysis was performed between OPCs versus OPCs lacking *Mettl14* and oligodendrocytes versus oligodendrocytes lacking *Mettl14*. In brief, exon-exon junctions from mapped RNA-seq reads, which are representative of introns that are removed from pre-mRNA, were extracted. Next, alternatively excised introns, which are comprised of two more overlapping introns (e.g., introns that share a splice site), were clustered together. Finally, differential intron excision events across conditions were tested using LeafCutter (Li et al., 2018).

QUANTIFICATION AND STATISTICAL ANALYSIS

All immunohistochemistry and electron microscopy data obtained from experimental and control mice were compared with a two-tailed unpaired Student's t test. Data were presented as mean ± SEM. A p value of less-than 0.05 was considered significant. Analysis was done using GraphPad Prism version 6.00 for Windows (GraphPad Software) and Microsoft Office Excel 2010.

DATA AND CODE AVAILABILITY

The sequencing data have been deposited to the National Center for Biotechnology Information Gene Expression Omnibus database under GEO: GSE124244.